



Graphene/silicon and 2D-MoS₂/silicon solar cells: a review

A. J. Wirth-Lima¹ · P. P. Alves-Sousa² · W. Bezerra-Fraga^{1,2}

Received: 4 February 2019 / Accepted: 3 March 2019
© Springer-Verlag GmbH Germany, part of Springer Nature 2019

Abstract

Due to the great interest in obtaining solar cells based on graphene/semiconductor Schottky junction and MoS₂/semiconductor heterojunction, in this review, we are presenting the technical details regarding those solar cells. For a better understanding of the technology used in the solar cells mentioned above, we initially show the graphene/semiconductor Schottky junctions and the adaptation of the thermionic theory to this type of junction. After this, we show the graphene/semiconductor Schottky junction solar cells and the MoS₂/semiconductor heterojunction solar cells. It is noteworthy that the understanding of this technology will serve as the basis for studies of more complex nanophotonic solar cells.

1 Introduction

The current photovoltaic devices (PN junctions) are composed of silicon with high purity, so that quite expensive manufacturing techniques are used. For this reason, there is currently a huge scientific effort to get solar cells based on other technologies with lower prices and, yet, with greater efficiency of conversion of solar energy into electric energy (power conversion efficiency—PCE).

Most likely, graphene is expected to replace the expensive ITO (indium tin oxide), or FTO (fluorine-doped tin oxide), which are used in solar cells for injection or charge collection. ITO has many disadvantages, such as high cost, since the element “indium” is very rare in the Earth’s crust and has high fragility, among other disadvantages.

One of the advantages of graphene is its high transparency in relation to electromagnetic radiation (including visible and ultraviolet), as well as excellent thermal conductivity, chemical stability, resistance to external forces and flexibility. In addition, graphene provides low sheet resistance, which can be controlled by its doping, or the number of layers. Therefore, the use of graphene in solar cells is of

enormous interest to the international scientific community that operates in this area of science [1, 2]. It is noteworthy that it has been shown that graphene used in photovoltaic devices has a few hundred Ω /square units and about 80% optical transparency [3].

The replacement of metal by graphene in solar cells based on metal/semiconductor Schottky junction causes greater absorption of photons so that more electron/holes pairs can be generated. Since electron/holes pairs are separated through the built-in electric field, these charges can be collected in the electrodes, generating electrical power. It should be noted that solar cells based on graphene/semiconductor Schottky junctions (GSSJ) are very promising, due to the low cost, simple manufacturing process and increasing competitiveness in relation to PCE.

It is worth mentioning that the production of graphene for use in solar cells is being elaborated in such a way that the imperfections are minimized, which also contributes significantly to the increase of the PCE value. Note that chemical doping of graphene is another option to obtain solar cells with greater PCE.

On the other hand, according to what is detailed throughout this work, molybdenum disulfide (MoS₂) is a semiconductor transition metal dichalcogenide (TMDC), whose atomic structure consists of a layer of molybdenum atoms (Mo) embedded between two layers of sulfur atoms (S), where the atomic bonds are covalent. However, each atomic structure referred above (every S–Mo–S layer) is connected to another layer through weak van der Waals force. MoS₂ bulk material has indirect band gap, but monolayer MoS₂ (Mo–S–Mo) has direct band gap, and the band gap value,

✉ A. J. Wirth-Lima
awljeng@gmail.com

¹ Department of Physics, Federal Institute of Education, Science and Technology of Ceará, Campus Sobral, Sobral, Ceará, Brazil

² Post-graduate Program in Electrical Engineering and Computing, Federal University of Ceará (U.F.C.), Sobral, Ceará, Brazil

optical absorption and carrier transport properties change according to the MoS₂ thickness [4]. It is worth noting that MoS₂ with a thickness of less than 1 nm can absorb between 5 and 10% of incident light [5]. In addition, MoS₂ can be synthesized with a large area by chemical vapor deposition (CVD) method.

Therefore, another option for obtaining solar cells with high PCE values is the use of MoS₂/silicon heterojunction.

In this review, we present the technical details regarding solar cells constituted by graphene/silicon Schottky junctions, as well as constituted by MoS₂/silicon heterojunctions, so that the reader can compare the performance of these two types of solar cells.

2 Graphene/semiconductor Schottky junction

Application of an external voltage changes the width of the depletion zone of the semiconductor, which becomes thinner when a forward voltage is applied and increases with the application of a reverse voltage, as can be observed in the equation below:

$$w = \sqrt{\frac{\epsilon_0 \epsilon_s}{qN} (V_{bi} - V - K_B T/q)}, \quad (1)$$

where ϵ_s is the dielectric constant of the semiconductor, q is the electron charge, N is the doping density, V_{bi} is the built-in potential, V is the applied external voltage and $K_B T/q = 26$ mV (due to its small value, this term can be neglected).

Since the value of metal density is high, an application of an external voltage at the metal/semiconductor Schottky junctions does not cause the Fermi level offset of metal. However, due to the limited density of states of the graphene, substitution of the metal with graphene provides charge transfer between graphene and semiconductor, which causes the displacement of the graphene Fermi level. It is worth mentioning that a transfer of 0.01 electrons per unit

cell provides a displacement of 0.47 eV of the Fermi level of the graphene [6].

On the other hand, without application of an external voltage, the graphene Fermi level does not move and we can then consider that it remains at Dirac point (ideal graphene) and in equilibrium with the Fermi level of the n-semiconductor (in this case), as shown in Fig. 1a.

Considering the application of an external voltage, the Fermi level of the metal at a metal (M)/semiconductor (S) Schottky junction remains unchanged, in view of its large density of states at the Fermi level. However, unlike what occurs with the Fermi level of the metal at an M/S Schottky junction, at a graphene (G)/semiconductor-n Schottky junction the Fermi level of the graphene is shifted downward during the application of a forward external voltage, due to the decrease in negative charges moving to the graphene, while the Fermi level of the n-semiconductor moves upward, in view of the lower concentration of positive charges in this said semiconductor, as shown in Fig. 1b. Note that the downward shift of the graphene Fermi level leads to an increase in its working function (in relation to the Schottky M/S junction) and consequently an increase of the potential barrier. In addition, the application of a forward external voltage causes the decrease of the value of the built-in potential, as can be seen in Fig. 1b. In this case, this displacement of the Fermi level of the graphene is small (it may not be considered), since the value of the direct voltage is usually small.

On the other hand, by applying a reverse external voltage at a G/S-n Schottky junction, the Fermi level for the graphene is shifted up significantly, while the Fermi level for the n-semiconductor is shifted downward, since in this case more positive charges are located in the semiconductor and more negative charges are transported to the graphene as shown in Fig. 1c. Note that unlike what occurs during the forward voltage application (the graphene working function and the potential barrier of the Schottky junction increase very little, while the value of the built-in potential suffers small reduction), during the application of a reverse voltage the value of the working function of the graphene as well as the potential barrier value significantly decreases. Note

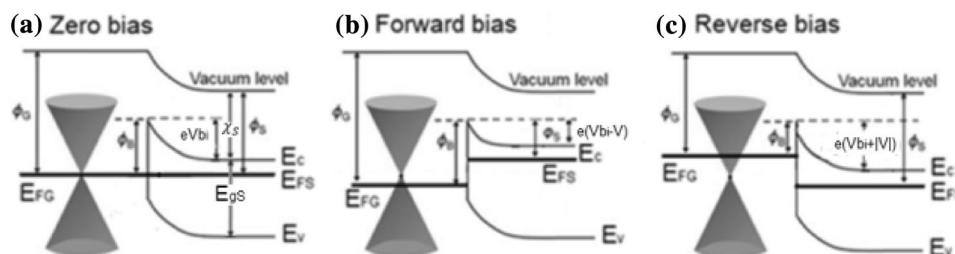


Fig. 1 **a** Energy band diagram for an ideal graphene/n-semiconductor Schottky junction without external voltage application. **b** Energy band diagram for an ideal graphene/n-semiconductor Schottky junction with application of forward external voltage. **c** Energy band diagram for an ideal graphene/n-semiconductor Schottky junction with application of external reverse voltage

that in this case, the value of the built-in potential increases. Therefore, the value of the potential barrier, during the application of a reverse voltage, depends on the value of the applied voltage (V) [7].

The influence of the graphene Fermi level variation (ΔE_{FG}), due to the application of an external electric field can be included in the thermionic model referring to the Schottky diode. In this case, the constant value of the potential barrier (ϕ_B) is replaced in equations referring to the reverse saturation current (I_0) and (V , I) curve by the variable value of the potential barrier ($\phi_B(V)$) (as a function of the applied voltage), according to Eqs. 2 and 3:

$$I_0(T) = AA^*T^2 e^{-\frac{\phi_B(V)}{k_B T}}; \quad (2)$$

$$I(T, V) = I_0 \left[e^{\left(\frac{qV}{\eta k_B T}\right)} - 1 \right]. \quad (3)$$

In Eqs. 2 and 3, A is the area of the Schottky junction, A^* is the Richardson constant ($A^* = 1.12 \times 10^6 \text{ A m}^{-2} \text{ K}^{-2}$ for n-Si), k_B is the Boltzmann constant ($1.38064852 \times 10^{-23} \text{ J/K}$), T is the temperature (K), q is the charge of the electron ($1.6 \times 10^{-19} \text{ C}$) and η is the diode ideality factor.

The width of the depletion zone at an M/S Schottky junction, as well as the electrons and holes locations at the Schottky junction, depends on the value of the applied external voltage (Eq. 1) and on the polarization type of this voltage, respectively.

It is worth mentioning that without application of an external voltage (Fig. 1a), there is the alignment of the Fermi bands, and in this case the charge density in semiconductor (the charge density in graphene has the same value) can be determined from Eq. 1 (considering $V=0$). Therefore, due to the application of an external voltage, the variation of the density of electrons located in graphene (n_i) at a G/S-n Schottky junction can be found according to Eq. 4. It is possible because the variation of the density of electrons in graphene is the same variation of the density of holes located in the n-semiconductor depletion region [7], i.e.,

$$n_{in} = -\Delta n_{dep} = - \left(\sqrt{[2\epsilon_0\epsilon_s N(V_{bi} - V - K_B T/q)]/q} - \sqrt{[2\epsilon_0\epsilon_s N(V_{bi} - K_B T/q)]/q} \right). \quad (4)$$

We can note that the second term on the right side of Eq. 4 represents the charge density transferred to the graphene without the application of external voltage. We can also notice that for forward voltage ($V > 0$), the value of n_i is positive so that graphene becomes positively doped (doped with holes, as shown in Fig. 1b). On the other hand, for reverse voltage ($V < 0$), the value of n_i is negative so that

graphene becomes negatively doped (doped with electrons, as shown in Fig. 1c).

In addition, we can use Eq. 5 (shown below) to determine the value of the variation of the Fermi level (or the chemical potential variation of graphene, $\Delta\mu_g$) [8, 9]:

$$\Delta\mu_g = \Delta E_F = \hbar V_F \sqrt{n_{in}\pi}. \quad (5)$$

Obviously, if we take into account the real graphene, we must insert the initial doping of graphene (n_0), which occurs due to the process of synthesis and transfer, interaction with the substrate and exposure to air, among other factors. In this case, the variation of the Fermi level is given by:

$$\Delta E_F = \hbar V_F \sqrt{|(n_0 + n_{in})\pi|} - \hbar V_F \sqrt{|n_0\pi|}. \quad (6)$$

Since the variation of Fermi level of the graphene corresponds to a potential barrier variation in the opposite direction, that is, $\Delta\phi_B(V) = -\Delta E_F(V)$, if we consider the potential barrier without application of an external voltage (ϕ_{B0}), the value of the V -dependent potential barrier is given by:

$$\phi_B(V) = \phi_{B0} + \Delta\phi_B(V) = \phi_{B0} - \Delta E_F(V). \quad (7)$$

Another way to change the position of the graphene Fermi level is via chemical doping using K and Ca atoms, as well as NH₃, O₂, and organic molecules, for example [10]. It is worth mentioning that the possibility of controlling the positioning of the Fermi level of graphene (unlike what occurs in metals, in which E_F is fixed) is an important advantage in the substitution of the metal with graphene, since in this way it is possible to control the Schottky barrier height (SBH) for a G/S Schottky junction (and the consequent rectification properties of the said Schottky junction).

In ideal graphene (without imperfections, chemical doping and application of external voltage, i.e., graphene has zero intrinsic charge density), the value of the Fermi level is located at Dirac points. However, since real graphene has non-zero intrinsic charge density, its Fermi level is not located at the Dirac point (the Fermi level is shifted up or down, depending on the type of doping). It is worth mentioning that according to the international scientific literature, the value of the graphene intrinsic charge density (n_0) can have typical values between $1 \times 10^{11} \text{ cm}^{-2}$ and $10 \times 10^{11} \text{ cm}^{-2}$.

It is noteworthy that the value of the applied gate voltage, which causes the position of the Fermi level to shift back to the Dirac points, is called Dirac voltage (V_D).

In a research carried out it was demonstrated that the dry transfer of graphene films to the standardized substrate (SiO₂/Si), as well as the subsequent cleaning through modified Radio Corporation of America (RCA) cleaning procedure, provides production of devices with low Dirac voltages related to graphene, i.e., $V_D < 4.5 \text{ V}$, with mean value being around 2.5 V [11]. Hence, considering that the value of V_D

depends mainly on the good quality of the graphene, we have adopted $V_D = 4.5$ V in our simulations.

3 Adaptation of the thermionic theory to the graphene/semiconductor Schottky junctions

Although graphene is a two-dimensional material, many studies are made using the equations referring to the metal/semiconductor Schottky diodes, which are obtained through the traditional thermionic emission model, without considering the physical characteristics inherent to graphene. Therefore, these equations are based on the charge carriers considered with mass, but in graphene these referred charge carriers are considered as massless. In addition, they do not take into account, for example, the influence of the Fermi velocity and the Fermi level on graphene.

The traditional Schottky diode equations are, for convenience, shown below:

$$J(T, V) = J_s(T) \left[e^{\left(\frac{qV}{\eta k_{B1} T} \right)} - 1 \right], \quad (8)$$

$$J_s(T) = A^* T^2 e^{-\frac{\phi_{B0}}{k_{B2} T}}; \quad A^* = \frac{4\pi q m K_{B1}^2}{h^3}. \quad (9)$$

However, it has been shown that in thermal equilibrium, the saturation current density ($J_s(T, E_F)$) and the current density flowing through the G/S Schottky junction as a function of temperature and polarization voltage ($J(T, V, E_F)$) are given by [12, 13]:

$$J_s(T, E_F) = A^* T^3 e^{-\frac{\phi_{B0} - E_F}{k_B T}}; \quad A^* = \frac{q K_{B1}^3}{\pi \hbar^3 V_F^2}, \quad (10)$$

$$J(T, V, E_F) = J_s e^{\left(\frac{-qV}{\eta k_B T} - 1 \right)}. \quad (11)$$

In the above equations, we include the terms $V_F = 10^6$ m/s (graphene Fermi velocity) and $E_F(V)$, i.e., the graphene Fermi level, which is dependent on the external voltage applied to the graphene. In addition, it was found that in this case, $A^* = 0.01158$ A cm⁻² K⁻³ for silicon, which is very close to the value found experimentally. The theoretical model shown above was experimentally tested using a diode with G/S Schottky junction, whose schematic representation is shown in Fig. 2 [12, 14].

Note that the Schottky diode consists of a set of nano-tips made in the silicon substrate in contact to graphene [14], which is in contact with the top electrode. However, this electrode is away from the Si due to a SiO₂ film.

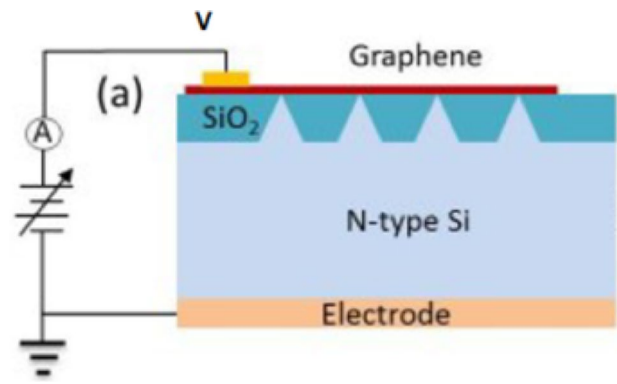


Fig. 2 Schematic representation of a G/S Schottky junction. (Adapted from Refs. [12, 14])

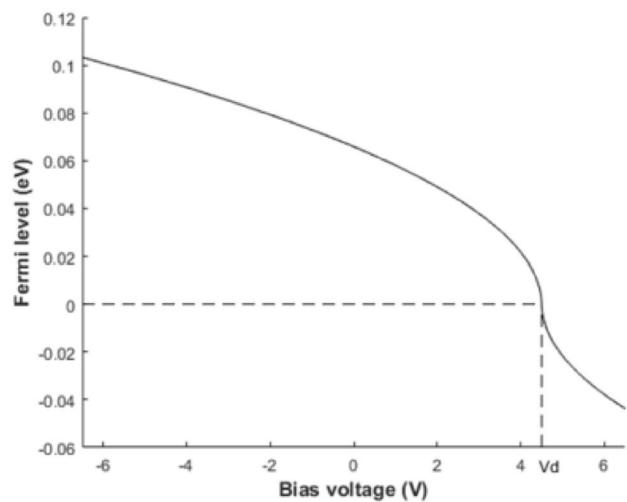


Fig. 3 E_F versus V

Graphene without the application of an external voltage has a non-zero Fermi level, due to intrinsic charge density, as previously detailed. For example, if we consider a flat structure constituted by an insulation layer between graphene and the doped semiconductor, the application of a gate voltage in the graphene causes a displacement of the graphene Fermi level given by [15]:

$$E_F = \pm \frac{\sqrt{1 + 2\alpha q |V - V_D|}}{\alpha}, \quad (12)$$

where the + signal is used for $V \leq V_D$ and the - signal for $V > V_D$, $\alpha = 2q^2 x / \epsilon_0 \epsilon_d \pi \hbar^2 V_F^2$, and $x = d - d_0$ is the effective distance between the charges in the graphene and in the semiconductor ($d = 300$ nm is the thickness of the dielectric and $d_0 = 0.24$ nm). In Fig. 3, we show the graph referring to the values of the Fermi level as a function of the applied

external voltage, taking into account the value of the Dirac voltage ($V_D = 4.5$ V as already detailed above).

It is worth mentioning that for forward voltage and $V > V_D$, the value of E_F is shifted downward, considering that the amount of electrons present in graphene decreases as a consequence of the reduction of the depletion zone, which leads to the reduction of the number of holes present in the depletion zone of the semiconductor (in this case, type n). On the other hand, in the case of the application of a voltage $V < V_D$ the depletion zone increases, causing the increase of the number of holes in the semiconductor, which entails in the increase of the amount of electrons in the graphene, so that in this case the value of E_F is shifted upward.

By means of other research it was found that the graphene/semiconductor interfaces, such as G/Si and G/GaAs, have inhomogeneities referring to the values of ϕ_{B0} , due to the reasons already mentioned above, where the dependence of ϕ_{B0} and of the ideality factor (η) as a function of temperature ($215 \text{ K} \leq T \leq 350 \text{ K}$) were examined [16]. These experiments have shown that ϕ_{B0} increases and η decreases with increase in the temperature, for G/Si and G/GaAs Schottky junctions. Assuming a Gaussian distribution of the potential barrier height (SBH), the values of ϕ_{B0} are 1.14 ± 0.14 eV and 0.76 ± 0.10 eV for G/Si and G/GaAs Schottky junctions, respectively. On the other hand, the values of η referring to the aforementioned temperature range vary from 2.62 to 1.66 and from 1.88 to 1.44, considering G/Si and G/GaAs, respectively. In addition, the Richardson constants for G/Si and G/GaAs (1.14×10^6 and $0.27 \times 10^4 \text{ A m}^{-2} \text{ K}^{-2}$, respectively) were determined [16].

4 Overview of solar cells based on graphene/semiconductor Schottky junction: solar cell parameters

The operation of a Schottky junction-based solar cell for the incidence of photons with energy $hf > E_g$ (E_g is the band-gap of the semiconductor, h is the Planck constant and f is the frequency of the photon) is possible, due to the built-in electric field in the depletion region. This is because, in the incidence of photons, the built-in electric field separates the

generated electron–hole pairs. After the charge separation in a G/n-semiconductor Schottky junctions, the electrons move toward the n-semiconductor, making it even more negative, while the holes are transferred to the graphene, making it positive (left part of Fig. 4).

Then, when this device is illuminated and the external circuit is open, a potential difference between its terminals (V_{oc}) arises, so that graphene receives holes (after the separation of charges due to the built-in potential) and becomes the positive terminal. Conversely, since the semiconductor receives electrons, it becomes the negative terminal.

By connecting the two terminals of this solar cell (short circuit) a current arises between these terminals, which is called short-circuit current (I_{sc}).

It is noteworthy that in a graphene-based Schottky junction solar cell, more light can reach the semiconductor and excite more electron–hole pairs. Hence, This will help the increase of the optical to electrical energy conversion efficiency.

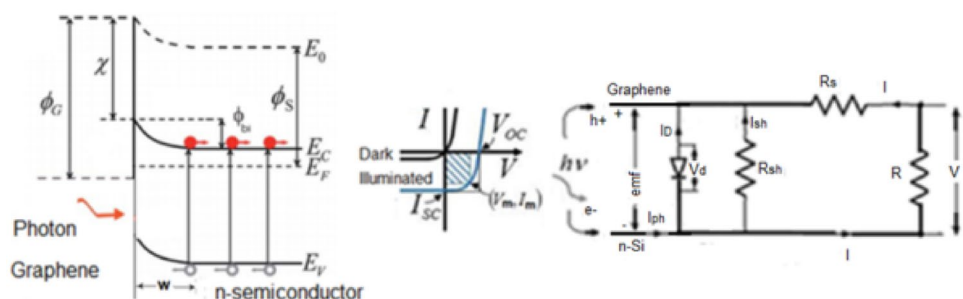
The characteristic curve (V , I) of this solar cell (without illumination and illuminated) is shown in the central part of Fig. 4.

On the right-hand part of Fig. 4, we can see the electrical circuit representing a solar cell based on Schottky junction, where it is shown that this solar cell is actually a current (or voltage) generator.

Considering the open circuit, due to the built-in potential, the photogenerated holes go to the terminal where the metal is located, while the electrons reach the semiconductor side (in this case n-Si). Therefore, the external circuit being open, the voltage called open-circuit voltage (V_{oc}) arises so that the electrode connected to the metal is the positive terminal and the electrode connected to the semiconductor is the negative terminal. In fact, V_{oc} is the value of the photogenerated electromotive force (emf).

On the other hand, the so-called short-circuit current (I_{sc}) arises by closing the external circuit. By inserting the resistance in the external circuit, the electrons flow through this resistance, and in this case we can obtain the I – V curve, which characterizes the solar cell. Note that in the external circuit, there is still a shunt resistance (R_{sh}) in parallel with the diode, as well as a series resistance (R_s), which is

Fig. 4 Left side: typical energy diagram for an illuminated graphene/n-semiconductor Schottky junction. Central part: characteristic (V , I) graph of an illuminated solar cell. Right part: equivalent electrical circuit relative to a solar cell based on graphene/n-semiconductor Schottky junction



caused by the resistivities of the semiconductor, graphene, and contacts. However, in most solar cells, the value of R_{sh} is very high and the value of R_s is too small, and these resistances are usually neglected. It is important to state that the Schottky junction in parallel with the electromotive force can be considered as a diode in which a forward bias is applied.

Very often, to consider the external current positive (I), the graph (V, I) can be transported to the first quadrant. In this case, the electric current in the external circuit, as well as the voltage between the terminals is given by:

$$I = I_{ph} - I_D - I_{sh}; \quad V = \text{emf} - V_{Rs}, \quad (13)$$

with I_{ph} being the generated photocurrent, I_D the current through the diode in forward bias (the built-in electric field has opposite direction to the electric field between the top electrode and the back electrode), I_{sh} the leakage current, emf the electromotive force produced in the solar cell, V_d the voltage at the Schottky junction and V_{Rs} the voltage between the terminals of R_s .

A disadvantage of solar cells based on M/S Schottky junctions is the open-circuit voltage related to the potential barrier so that the V_{oc} value of this type of solar cell is less than the value relative to the PN junctions-based solar cells.

However, the substitution of the metal by graphene or the use of heterojunctions is worldwide being researched, and it is believed that solar cell with higher PCE value than PN junctions-based solar cells will be obtained.

The generated photocurrent density (J_{ph}) in a solar cell is given by [17]:

$$J_{ph} = \int_{\lambda_1}^{\lambda_2} qT(\lambda)\Phi_{in}(\lambda)(1 - e^{-\alpha(\lambda)w}) d\lambda, \quad (14)$$

where λ_i are the maximum and minimum wavelengths of incident radiation range, $T(\lambda)$ is the graphene transmittance, $\Phi_{in}(\lambda)$ is the incident photon flux, $\alpha(\lambda)$ is the optical absorption coefficient of the semiconductor and w is the width of the depletion zone. It is worth mentioning that there is still the contribution to the current photo provided by the minority carriers, that is, the charge generated in the near-neutral zone of the substrate (and not recombined), which can be diffused to the depletion zone.

The relation (V, I) for the solar cell with ideal Schottky G/S Schottky junction ($R_s = 0$; $R_{sh} = \infty$ and $\eta = 1$) can be obtained from Eq. 13, via thermionic emission theory, given by:

$$I = -(I_{ph} - I_D) = I_0 \left[e^{\left(\frac{qV}{k_B T} \right)} - 1 \right] - I_{ph}. \quad (15)$$

Note that the generated photocurrent (I_{ph}) shifts the characteristic curve (V, I) to the fourth quadrant, where the voltage is positive, but the current is negative. In this way, the

power absorbed by an illuminated solar cell supplies electrical power to the external circuit. However, for a real solar cell, the relation (V, I) is obtained as follows:

$$I(T, V) = I_0 \left[e^{\frac{q(V-R_s I)}{\eta k_B T}} - 1 \right] + \frac{V - R_s I}{R_{sh}} - I_{ph}, \quad (16)$$

which can be solved numerically.

From Eq. 16 it is possible to obtain I_{sc} and V_{oc} , for $V=0$ and $I=0$, respectively, for a solar cell with high quality, i.e., it has R_s with a small value and R_{sh} with a high value, according to the following equations:

$$I_{sc} \approx -I_{ph}; \quad V_{oc} \approx \frac{\eta k_B T}{q} \ln \left(\frac{I_{ph}}{I_0} + 1 \right) \approx \frac{\eta k_B T}{q} \ln \left(\frac{I_{ph}}{I_0} \right). \quad (17)$$

In addition, V_{oc} can be determined by replacing I_0 by Eq. 2, as follows [7]:

$$V_{oc} = \frac{\eta k_B T}{q} \ln \frac{I_{ph}}{AA^* T^2} + \frac{\eta}{q} \phi_B. \quad (18)$$

As we can see in Eq. 18, the value of V_{oc} grows in proportion to the growth of the value of ϕ_B .

Considering that the values of η , I_{ph} , I_0 , R_s , and R_{sh} depend on the dimensions and physical characteristics of the solar cell, Eq. 16 can be replaced by:

$$J(T, V) = J_0 \left[e^{\frac{q(V-R_s J)}{\eta k_B T}} - 1 \right] + \frac{V - R_s J}{R_{sh}} - J_{ph}, \quad (19)$$

where J , J_0 , and J_{ph} are the densities of electric current, saturation electric current and generated photocurrent, respectively.

The (V, I) solar cell graph can be produced very simply by using sunlight itself, or in a laboratory. However, solar simulators should be used under conditions that comply with the air mass (AM) standard. There are several AM standards, such as AM1, which determine the solar spectrum parameters for an incidence of sunlight from 90° above the horizon, i.e., from the zenith, as shown on the left part of Fig. 5.

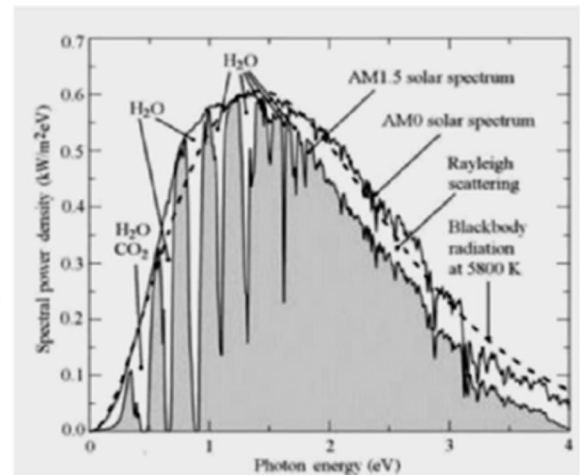
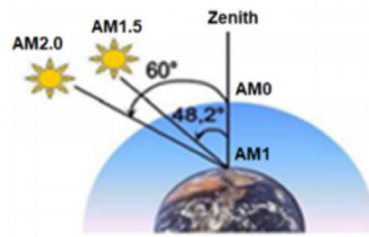
If we consider the Sun localized at an angle $z < 80^\circ$ from the zenith (or an angle $h > 10^\circ$ from the horizon), AM is defined as:

$$AM = \frac{1}{\cos(z)} = \frac{1}{\sin(h)}. \quad (20)$$

AM1.5 is generally used in simulations of solar cells, where the angle $z = 48.2^\circ$, according to Eq. 20, which represents the measurements in tropical regions. The typical parameter values used in AM1.5 are: irradiance $G^R = 1000 \text{ W/m}^2$ and temperature $T = 25^\circ \text{C}$.

The solar radiation spectrum has a frequency distribution similar to that of a black body at a temperature of

Fig. 5 Left part: position of the Sun referring to AM0, AM1.0, AM1.5 and AM2.0. Right part: graphical representation of the spectrum of solar radiation according to AM0, and AM1.5



5800 K (approximately, the surface temperature of the Sun). However, during the passage of these radiations through the Earth's atmosphere, this spectrum of solar radiation suffers the effects of reflections in the clouds, absorptions and diffusions. In addition, these radiations undergo diffraction caused by pure and dry gases, which have spherical particles smaller than one-tenth of the wavelength ($r < 0.1\lambda$), so that these diffractions behave similarly to what is described in the Rayleigh scattering theory. There is still the attenuation or extinction of certain wavelengths when the solar radiations cross the atmosphere. This is due, for example, to the absorption by ozone (O₃), carbon dioxide (CO₂), oxygen (O₂) and water vapor (H₂O).

The spectral distributions (or spectral irradiances) associated with the test conditions AM1.5 and AM0 are shown in the right part of Fig. 5.

The solar radiation has a spectral range from 100 to 3000 nm, with a maximum spectral density at 550 nm, which corresponds to yellowish-green light. Note that the atmosphere changes the spectral distribution of the light that passes through it, attenuating (and even annihilating) the intensity of its components.

This spectrum has a direct impact on the photogenerated current, according to the spectral response of the cell, which depends on the response of the semiconductor material from which it is made. For example, silicon has its peak response in the near infrared (900 nm) region, reaching red in the visible region (740 nm).

A figure of merit widely used in solar cell technology is called fill factor (FF), given by:

$$FF = \frac{I_m V_m}{I_{sc} V_{oc}}. \quad (21)$$

As we can see in the central part of Fig. 4, V_m and I_m are the voltage and current values, respectively, that provide

the maximum value of the electric power generated by the solar cell. Hence, the FF value represents how close the $V_m \times I_{max}$ rectangle area is to the area of the rectangle defined by $V_{oc} \times I_{sc}$. Typical values of FF are in the range of 70–85%, depending on the structure of the solar cell.

The power conversion efficiency (PCE) is defined as the ratio between the maximum power generated by the solar cell and the power of the incident solar light, i.e.:

$$\eta = \frac{I_m V_m}{P_{in}} = \frac{I_{sc} V_{oc} FF}{P_{in}}. \quad (22)$$

In Eq. 22, P_{in} is the incident optical power (do not confuse the parameter η referring to the PCE with the ideality factor parameter).

It is noteworthy that there is also the external quantum efficiency (EQE), also called incident photon-to-electron conversion efficiency (IPCE), which determines the number of charges generated due to the number of incident photons, given by:

$$EQE = \frac{I_{ph}/q}{\Phi_{in}} = \frac{I_{ph} hf}{q P_{in}}, \quad (23)$$

with $\Phi_{in} = P_{in}/hf$ being the incident photon flux (number of photons reaching a given area over a given period of time). The ideal value of EQE is 1 and the reduction of this value occurs due to the loss of current as a function of the amount of recombination, absorption efficiency, reflections, etc. On the other hand, internal quantum efficiency (IQE) is defined as the ratio between the number of charge carriers collected by the solar cell and the number of photons that are absorbed by the solar cell. The value of IQE is determined in a similar way to that adopted for the determination of the EQE, but in this case only the flow of absorbed photons ($\Phi_{abs} = \alpha \Phi_{in}$) is considered, with α being the semiconductor absorbance. Therefore, the IQE value can be determined as follows:

$$\text{IQE} = \frac{I_{\text{ph}}/q}{\Phi_{\text{abs}}} = \frac{I_{\text{ph}}hf}{\alpha q P_{\text{in}}}. \quad (24)$$

Therefore, all the incident photons on the cell surface are considered in the EQE value, but only the absorbed photons are considered in the IQE value.

In addition to the aforementioned parameters, there is also the spectral response in relation to the photocurrent (R_I), that is, the ratio between the value of the generated photocurrent and the value of the incident optical power, given by [18]:

$$R_I = \frac{I_{\text{ph}}}{P_{\text{in}}} = \frac{q\lambda\text{EQE}}{hc} \quad (\text{A/W}), \quad (25)$$

as well as the responsiveness in relation to photovoltage, given by:

$$R_V = \frac{V_{\text{ph}}}{P_{\text{in}}} \quad (\text{V/W}). \quad (26)$$

Note that the relation between spectral response and external quantum efficiency (R_I), can be determined from the spectral response by replacing the optical power at a particular wavelength with the photon flux related to this wavelength.

Remember that using the usual signal convention, the absorbed power is negative, i.e., the solar cell supplies power to the external circuit. However, for applications in photovoltaic cells, often by convention, the current supplied by the cell is adopted with positive value. In this case, the values referring to the I axis of the (V, I) graph are transported to the first quadrant. In addition, solar cell manufacturers often provide the parameters inherent to their devices, such as V_{oc} , I_0 , V_{m} , and I_{m} , among others. Then, from some of these parameters, it is possible to determine the other parameters. For example, from Eq. 17, it is possible to find the value of I_0 , which is given by:

$$I_0 = \frac{I_{\text{sc}}}{\left(e^{qV_{\text{oc}}/\eta K_B T} \right)}. \quad (27)$$

Therefore, knowing the values of V_{oc} and I_{sc} , from Eq. 16 (neglecting R_s and R_{sh} parameters), we obtain:

$$I = I_{\text{sc}} - \frac{I_{\text{sc}}}{\left(e^{qV_{\text{oc}}/\eta K_B T} \right)} \left[e^{\left(\frac{qV}{\eta K_B T} \right)} - 1 \right]. \quad (28)$$

Moreover, using the equation $P = V \times I$ and considering the values V_{m} and I_{m} , which provide the maximum power value (P_{m} , where $dP/dV = 0$), we can find the following mathematical expression for the determination of the value referring to the ideality factor:

$$\eta = \frac{q(V_{\text{max}} - V_{\text{oc}})}{K_B T \ln \left(1 - \frac{I_{\text{max}}}{I_{\text{sc}}} \right)}. \quad (29)$$

In addition, as it was explained above, the PCE (η) is defined as the quotient between the maximum power, P_{m} , and the power of incident radiation (P_{in}):

$$\eta = \frac{P_{\text{m}}}{AG}, \quad (30)$$

with A being the active area and $G = 1000 \text{ W/m}^2$ the value of the solar radiation power under AM1.5 conditions.

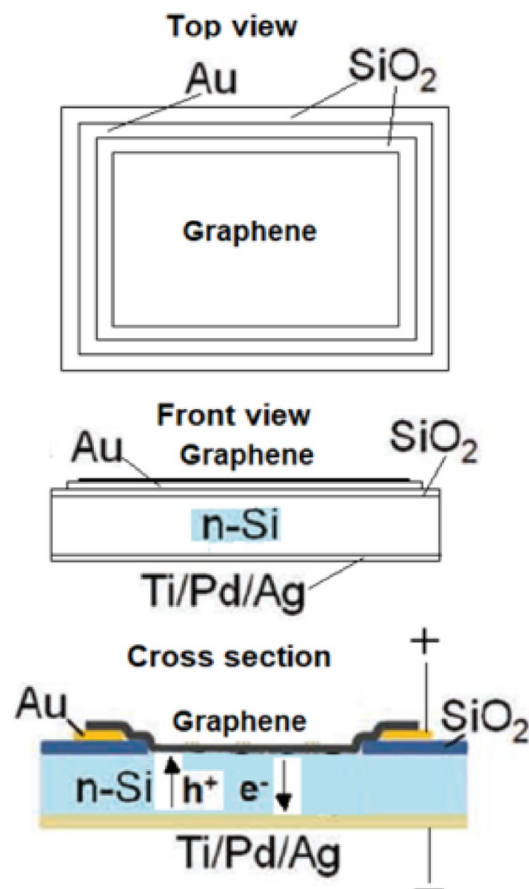


Fig. 6 Schematic representation of a solar cell based on G/n-Si Schottky junction. (Adapted from Ref. [19])

5 Nanophotonics solar cells made up of graphene/n-silicon Schottky junction

Figure 6 shows the schematic representation of one of the first presented solar cells constituted by a G/n-Si Schottky junction, which has a low PCE ($1.0\% \leq \eta \leq 1.7\%$) [19].

Note that a thin film of graphene was placed on an Si/SiO₂ substrate, the SiO₂ layer window area being 0.1 cm² and 0.5 cm² (to allow contact of the graphene film with n-Si). As we can see, the contact electrode (Au) is inserted between the SiO₂ layer and the graphene film. Scanning electron microscopy (SEM) revealed that the surface of the graphene film is smooth, but with roughness, the graphene film has good contact with the Au layer and the SiO₂ layer has good contact with the Si layer. In addition, it was verified that the graphene film was composed of layers of graphene, which were superposed and interconnected to ensure the continuity of the film, even if there were cracks in one of the layers. Moreover, these multiple layer structure of graphene has high mobility value [20]. The thickness of the SiO₂ layer is 300 nm and the silicon doping (N_D) has value between $1.5 \times 10^{15}/\text{cm}^3$ and $3.0 \times 10^{15}/\text{cm}^3$.

Considering that the depletion region and the built-in potential are located close to the G/n-Si interface, we can assume that graphene besides working as a transparent electrode, also works as an active layer for the separation of electrons and holes and still provides the transport of holes. Then, the electrons that reach the conduction layer are transferred to the back electrode and the holes are transferred to the metal electrode in contact with the graphene.

Considering that the work function of graphene (Φ_G) has a value between 4.8 and 5.0 eV and the working function of Si ($\Phi_{n\text{-Si}}$) has a value of 4.25 eV, the built-in field has a relatively high value ($0.55 \text{ eV} < V_0 < 0.75 \text{ V}$). It was also verified that the potential barrier has a value $\Phi_b \approx 0.78 \text{ eV}$, which is according to $\Phi_G - \chi = 0.75 \text{ eV}$ since $\chi = 4.05 \text{ eV}$.

The (V , J) curves for the devices with area $A = 0.1 \text{ cm}^2$ and 0.5 cm^2 were obtained (according to the reference AM1.5) and the PCEs were $\eta = 1.65\%$ and $\eta = 1.34\%$, respectively. These values are close to those previously disclosed, which showed open-circuit voltage V_{oc} between 0.42 and 0.48 V, short-circuit current density J_{sc} between 4 and 6.5 mA/cm², and fill factor FF between 45 and 56%, which corresponds to PCE with a value between 1 and 1.7%.

The values of the PCEs referring to these devices should be increased through a better-elaborated production of the respective Schottky junctions, as well as the use of silica surface passivation. It is worth mentioning that graphene acts as an anti-reflection layer, reducing the reflection in approximately 80% in the near infrared frequency band and about 70% in the visible light frequency region.

It was also observed that the IPCE increases rapidly for incident photons with energy higher than 1.0 eV, has a peak value for incident photons with energy around 1.5 eV, and decreases more slowly as a function of the increase of the photon energy (higher than 1.5 eV).

The width of the depletion region was determined by the following equation:

$$W = \sqrt{\left(\frac{2\epsilon_0\epsilon V_0}{qN_D} \right)}, \quad (31)$$

with $\epsilon = 11.9$ being the dielectric constant of silicon, q the electron charge, N_D the value of the doping of silicon and V_0 the value of the built-in field. The width of the depletion region of this solar cell was estimated between 0.5 and 0.7 μm . The increase in the IPCE value will be possible through the use of graphene films having greater uniformity, since in this way it is possible to obtain better separation of charges and transport of holes, as well as to avoid the recombination of charge carriers.

The value for the resistance of a series of solar cells presented values between 9 and 12 Ω , for the voltage range between 0.1 and 2.0 V and the value of the shunt resistance showed a value of up to 45 M Ω (determined through the (V , I) curve for reverse voltages). According to the measurements made using reverse voltages, it was verified that damage of the G/-Si-n Schottky junction occurs for voltage of approximately 30 V.

Further researches on graphene/silicon-based solar cells revealed that by controlling the number of graphene layers, the proper work function of graphene and the addition of antireflection film, it is possible to obtain a conversion efficiency of 9.2% for this type of solar cell. In addition, the use of modified graphene films and silicon columns forming the Schottky junction provided graphene/silicon solar cells with an efficiency of up to 7.7% [21].

The solar cells studied in this research were manufactured by the researchers and simulated using the parameters extracted from their measurements and experiments. In addition, the researchers developed analytical theories focused on the work function, as well as on the number of layers of graphene. In one of the stages of the simulations and analyses, the insertion of an antireflection layer was analyzed, to maximize the effects related to the incidence of sunlight in the semiconductor.

It is noteworthy that the control of the graphene work function (Φ_g) can be controlled by the application of gate voltage, or by the insertion of chemical doping so that the values of Φ_g can be between 3.5 and 5.1 eV [22–24].

The reason for the control of the work function of the graphene occurs due to the fact that a larger value of Φ_g provides the increment of the value related to the built-in

potential and, as a consequence, the generation of charges in the solar cell increases. In addition, the correct choice of the number of layers of the graphene allows a greater efficiency regarding the film resistance and the transmittance of this material.

On the other hand, the insertion of the antireflection layer causes the reduction of the reflection of the light incident on the silicon, since without this antireflection layer the reflection is greater than 35%, for wavelengths between 350 and 800 nm [25].

However, the technique used to obtain antireflection was different from the conventional one. In this case, a pillar array (PA) was inserted in the silicon area in contact with the graphene, which was made using the common process of lithography and etching. It is noteworthy that using this anti-reflective structure the reduction of the reflectance was approximately 0.01%, considering the AM1.5 conditions.

To compare the efficiency of the studied solar cells, solar cells made of modified graphene and/or PA films were fabricated and tested as will be detailed later [21].

The following equations were used during the theoretical analysis:

$$J' = J_0 \left[e^{\left(\frac{qV'}{\eta k_B T} \right)} - 1 \right] - J_{ph}; \quad (32)$$

$$\begin{bmatrix} V \\ J \end{bmatrix} = \begin{bmatrix} 1 + R_s/R_p & R_s \\ 1/R_p & 1 \end{bmatrix} \begin{bmatrix} V' \\ J' \end{bmatrix}, \quad (33)$$

where R_s and R_p are the resistances, in series and in parallel (causes the leakage current in the Schottky junction, due to the poor quality of the insulation between the top electrode and the substrate, or due the tunneling effect at said junction), respectively, J' and V' represent the current density and

voltage, respectively, of the solar cell without the effects of the resistances, and J and V represent the current density and voltage, respectively, of the actual solar cell.

Taking into account that these solar cells are based on Schottky G/S junctions, the value of the potential barrier with no incidence of sunlight (in the dark) is given by $\Phi_{B0} = \Phi_G - \chi$, as already detailed previously.

The graphene resistance can be determined via $R_G = kR_{sh}$, where R_{sh} is the film resistance of the graphene and k is a proportionality factor with a value dependent on the geometry of the solar cell. The value of R_{sh} is given by:

$$R_{sh} = \frac{1}{q(\mu_e N_e + \mu_h N_h)}, \quad (34)$$

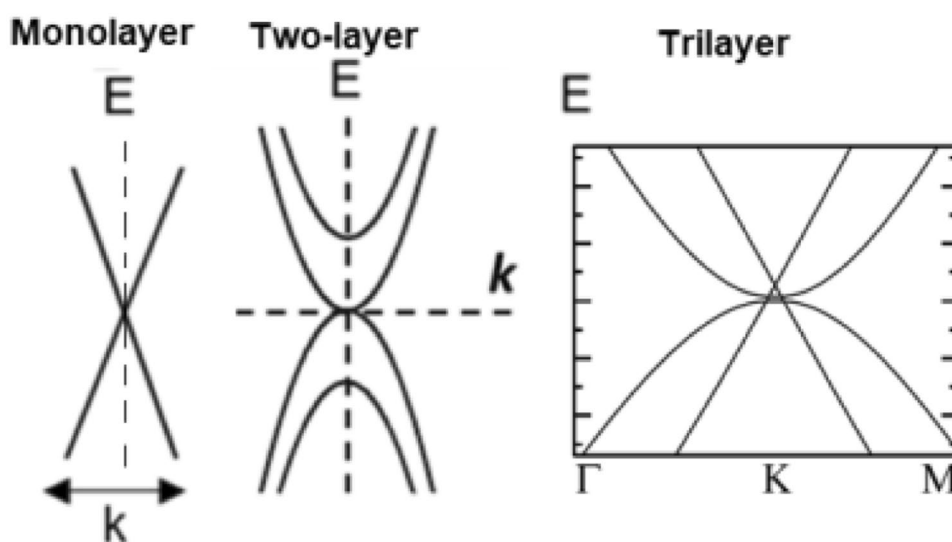
where μ_e and μ_h are the electron and hole mobilities in the graphene, respectively, and N_e and N_h are the electron and hole densities, respectively.

The graphene dispersion relation depends on the number of layers, as been obtained through various researches. Monolayer, two-layer and an example of trilayer graphene dispersion relations (k , E) are shown in Fig. 7 (values close to the Dirac point).

Note that the dispersion relation of graphene with more than one layer in the vicinity of the Dirac point is not linear.

It is worth noting that the physical properties of solar cells with PA were determined considering this PA as a stratified flat dielectric film, having several equivalent refractive indices in the direction of its thickness [25]. Moreover, the values of some experimental parameters, such as ideality factor (η) and dimensional proportionality factor (k), were used. Since the (V , J) curve obtained in the analytical method was similar to the (V , J) curve obtained experimentally, the validity of the presented theoretical model was proved.

Fig. 7 Graphene dispersion relations for one, two and three layers (top, center and bottom, respectively)



Graphene synthesis was performed using a typical CVD method using catalytic substrates (copper), which are placed in a quartz tube (reactor), mounted in a tubular furnace, and with methane used as the precursor. Before graphene growth, the tube was purified with argon and after that heated to 1000 °C in a mixture of argon–hydrogen (200:5 ml/min). After this step, a methane flow was inserted into the quartz tube, the methane–hydrogen–argon mixture being 10:2:200 ml/min. After graphene growth, the copper was removed and the furnace was cooled under a hydrogen–argon atmosphere. The graphene film was then separated from the copper by the use of an aqueous solution of iron perchloride (FeCl₃).

A layer of SiO₂ with a thickness of 300 nm was deposited on a silicon(100) n-type substrate, which acted as an insulator between the silicon and the top electrode. This top electrode (Ti/Au), as well as the back electrode (Ti/Pd/Ag), was obtained via electron-beam physical vapor deposition. After this step, the pillar arrays were produced by photolithography and dry-reactive-ion etching (RIE) method. The graphene obtained through CVD was then placed on the PA area, where the effective area of illumination of the solar cell has a value of 0.1 cm² and pillars have a diameter of 1.9 μm, and height between 200 nm and 1 μm. Figure 8 shows the schematic representation of the solar cell G/n-Si with the pillar arrays [21].

Modification of the graphene via HNO₃ was performed by exposing it to fuming HNO₃ and the thus produced graphene/n-Si solar cells were placed above a fuming HNO₃-containing flask (65% by weight). To avoid corrosion

of the silver and the underlying Si, the treatment time was carefully controlled.

The solar cells manufactured as detailed above were tested with a solar simulator (“Newport”) under AM1.5 conditions, and the current and voltage data were obtained via the “Keithley 2602” measuring instrument.

In summary, the studies and simulations of the above-mentioned solar cells have shown that the following steps are necessary to improve the efficiency of these solar cells. Reduction of the reflectance of the conventional graphene/silicon Schottky junction (around 35%): to overcome this problem the above-detailed anti-reflection technique was used; reduction of the parasite resistance, to avoid the dissipation of the converted electric energy and increase of the built-in potential and to increase the efficiency of the charges (electrons/holes) separation process. The solution found to minimize these two latter problems was the careful determination of work function and the number of layers of graphene.

Among several models of solar cells that were simulated and analyzed, the one that presented the highest values related to the graphene work function ($\Phi_G = 5.1$ eV), open circuit voltage ($V_{oc} = 0.84$ V), current density ($J_{sc} = 16.1$ mA/cm²), fill factor (FF = 68.2%) and PCE ($\eta \approx 9.2\%$) composed of two layers of graphene, doped via AuCl₃ [26], and this solar cell also has PA.

However, even more recent research has revealed the achievement of a solar cell also based on the G/n-Si Schottky junction, in which the back contact structure was changed. In addition, this solar cell has a simpler manufacturing process, low manufacturing cost, as well as a contact area greater than that presented by solar cells of this type.

Additionally, it was found that poly(methyl methacrylate)—PMMA residues (which occurs by the polymerization reaction of the methyl methacrylate—CH₂=C(CH₃) COOCH₃ monomer used during the deposition of the graphene on the substrate) left in the graphene during this transfer process should be removed as much as possible to eliminate the s-shape in the (V , J) curves, thus increasing the conversion efficiency of this solar cell. It is noteworthy that this type of solar cell has conversion efficiency $\eta = 10\%$ for graphene/Si textured structure, without chemical doping and anti-reflection coating, and this conversion efficiency is increased to $\eta = 14.1\%$, after the application of chemical doping in graphene. Moreover, these solar cells with doped graphene presented great stability and retain 84% of their conversion efficiency, after 9 days in air.

At the top of Fig. 9, we show the schematic representation of this mentioned solar cell [27].

In the central part of Fig. 9, we can see that the light falls directly on the silicon substrate so that the full use of the active zone is reached. It is possible because the metal grid is located at the bottom of this solar cell.

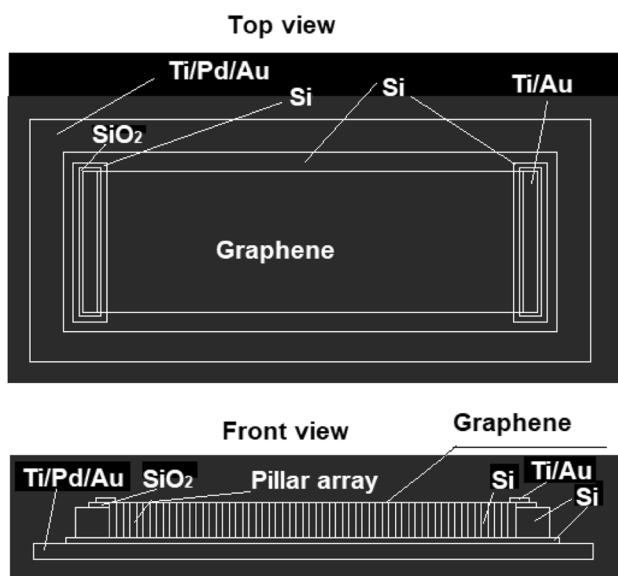


Fig. 8 Schematic representation of the solar cell constituted by G/n-Si/PA

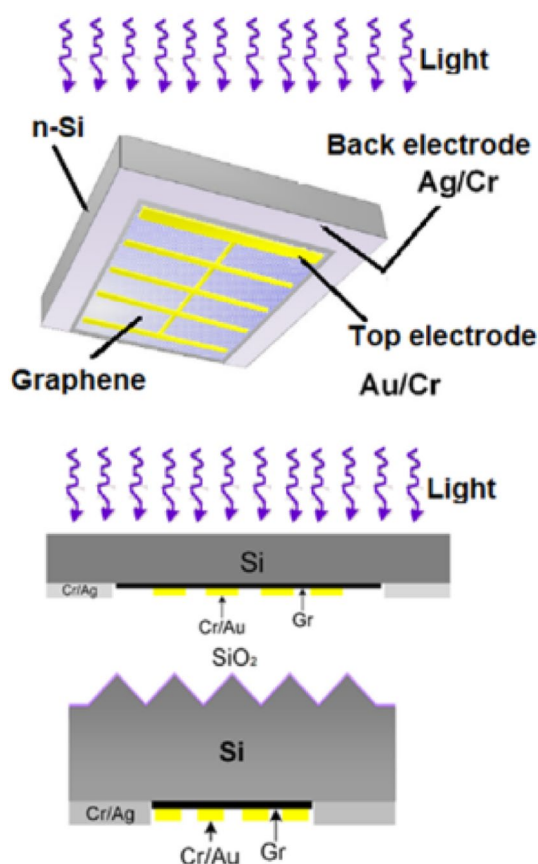


Fig. 9 Top: schematic representation of the presented solar cell. The light penetration occurs through the back electrode and reaches the graphene/n-silicon-n Schottky junction. Center: schematic representation of the cross section of the solar cell. Bottom: schematic representation of the location of the silicon texturing and passivation layer (SiO_2). Adapted, from Ref. [27]

At the bottom of this figure, the silicon texturing and passivation (SiO_2 layer) located at the top of the silicon substrate is shown, which provides the reduction of the reflectance.

To achieve the texturization of the single-crystalline-silicon (c-Si) substrate surface (n-Si(100)), which has resistivity between 2 and $3 \Omega/\text{cm}^2$, 0.19 cm^2 contact area, and a thickness of $200 \mu\text{m}$, its cleaning was done with a solution of $\text{NH}_4\text{OH}:\text{H}_2\text{O}_2:\text{H}_2\text{O}$ (1:1:5) for 10 min. Thereafter, the substrate is immersed in a solution of potassium hydroxide—KOH (25% by weight) for 2 min to remove the residues. Next, a solution with 200 ml of KOH/IPA/DI H_2O is used, to obtain the texturing of the silicon and consequently a reduction of the reflectance on the silicon surface. In fact, four different concentrations of isopropyl alcohol, i.e., IPA (“Isopropyl alcohol”— $\text{C}_3\text{H}_8\text{O}$) by volume and KOH concentration (1% by weight) were used. The concentration of IPA that caused the highest average reflectance (28%) was

4% by volume. This stage lasts for 45 min at a temperature of 75°C .

The manufacture of this solar cell has the following steps:

1. The silicon substrate (textured or non-textured) is cleaned by RCA procedures to eliminate metal ion contamination and immersion of this substrate in a 2% HF solution diluted for 30 s, to remove the oxide layer. After this, the process of passivation of the silicon surface, exposing the silicon substrate in the ambient air, during the time interval of 2 h [28–30] is elaborated.
2. The graphene/PMMA layer is deposited over the central area of what will be the bottom of the solar cell [31]. The area of the graphene layer is $3.3 \times 3.3 \text{ mm}^2$, obeying the recommendations to obtain a solar cell with high efficiency [28, 32]. Prior to removal of the PMMA layer (by acetone treatment), a treatment called deep UV treatment (DUV) is applied (illumination of the surface with deep ultraviolet ray (254 nm at 180°C) between 30 and 60 min). This treatment allows the maximum possible removal of PMMA residues [31] and provides enhancement of graphene p-doping.
3. The back electrode is then created via deposition of Cr/Ag layers on the substrate (unpolished side). Then, the top electrode in the shape of a grid (Cr/Ag) is created on the graphene layer, which provides low contact resistance in relation to this layer of graphene [30, 33, 34].
4. To obtain p-type doping of the graphene, a solution with 65% of HNO_3 is applied for 60 s.

The solar cell obtained through this process has an active area with a value equal to 0.19 cm^2 , therefore greater than the active area of the solar cells produced in previous researches, which represents a greater absorption of photons and consequently a greater efficiency of conversion of energy. In addition, the texturization of the silicon obtained during the manufacture of this solar cell is applied only at its top, so that the graphene is deposited directly onto the non-textured part of the silicon substrate. Therefore, this procedure should avoid the process of recombination of charge carriers, which usually occurs between graphene and the textured surface of the silicon substrate.

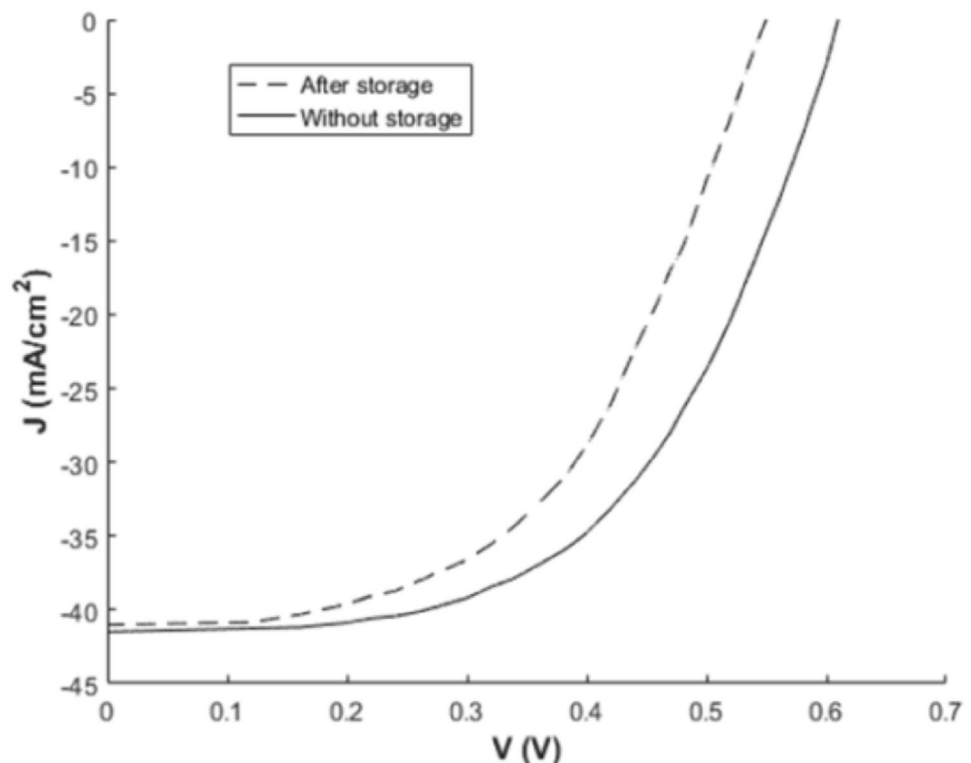
X-ray photoelectron spectroscopy (XPS) was used, for the determination of the amount of PMMA residues in the graphene after its transfer. The used instruments were Kratos AXIS Ultra DLD spectrometer; Al $\text{K}\alpha$ monochromatic photon emitter (in the X-ray region with an energy of 1486.6 eV , operating power 150 W).

The above-mentioned solar cells were calibrated through a standard solar cell and their parameters were determined through measurements via Keysight B1500A Semiconductor Analyzer, using a solar simulator under conditions AM1.5, with an illumination intensity of $100 \text{ mW}/\text{cm}^2$.

For the determination of the external quantum efficiency (EQE) of these solar cells, a PVE300 system was used.

It was demonstrated during the experiments that the PMMA residues cause a kind of trap of the photogenerated charge carriers during their movements through the interface, causing an increase in the amount of electron/holes recombination. In addition, previous experiments have shown that these residues interfere with the separation process of photogenerated charges, obtained by the actuation of the built-in potential [35]. Briefly, it was found that the DUV treatment results in the maximization of the reduction of PMMA residues and the consequent increase in the value of the short-circuit current density (J_{sc}), as well as a small decrease in the open circuit voltage (V_{oc}), i.e., it causes a decrease in p-type doping of graphene [31, 36]. However, the increase of the duration of DUV treatment beyond 20 min causes the increase of p-doping of graphene, so that graphene becomes a high-quality monolayer [37]. On the other hand, it has been proved by XPS measurements and Raman spectroscopy that DUV treatment periods longer than 60 min imply the decay of graphene quality so that the duration of this treatment should be between 20 and 60 min. Therefore, the reduction of the residues leads to the elimination of the *s* format in the (V , J) curve of the solar cells based on graphene/n-silicon Schottky junction. In addition, it has been proven that the increase of the active area of this solar cell provides an increase in the value of PCE (compared to solar cells that have less active area).

Fig. 10 (V , J) curves referring to the solar cells mentioned above, considering the degradation due to exposure to the environment and without taking into account this said degradation



The use of the textured substrate reduced the reflectance to 13% in the wavelength range between 400 and 700 nm. Finally, applying a solution with 65% of HNO₃ for 60 s after the implementation of p-type doping of graphene, the measured parameters of the solar cell were: J_{sc} = 40.8 mA/cm²; V_{oc} = 0.61 V; FF = 57% and η = 14.1%. However, exposing this solar cell to ambient conditions, it was observed that after 9 days, changes occur in the values mentioned above, due to the gradual evaporation of the dopants [38, 39], so

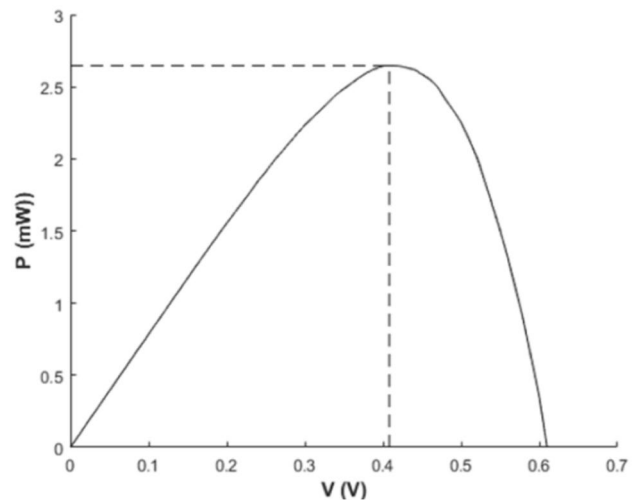


Fig. 11 (V , P) curve

that the PCE value decreases to 11.83% [27], but after these 9 days, the values remain practically unchanged.

Based on the data and (V, J) curves taken from these surveys, we elaborated analytically the (V, J) curve referring to the solar cell that does not come into contact with the environment and to that which remains exposed to the environment (Fig. 10).

Considering what was detailed above and using the values provided by the researchers ($J_{sc} = 40.8 \text{ mA/cm}^2$, $V_{oc} = 0.61 \text{ V}$, $FF = 57\%$ and $\eta = 14.1\%$), we determined the maximum power value of the solar cell ($P_m = 2.646 \text{ mW}$), as well as the values of $V_m = 0.408 \text{ V}$ and $I_m = 6.479 \text{ mA}$ (Fig. 11).

We also calculate the value of $\eta = P_m/P_{in}$, whose value is very close to that presented by the researchers.

It is important to note that, since graphene work function can be altered in several ways, such as via doping, the graphene/semiconductor potential barrier can also be altered.

To complement this section, the graphs (V, P) referring to four solar cells with the following parameters are shown in Fig. 12: $V_{oc} = 0.65 \text{ eV}$, $I_{sc} = 8 \text{ mA}$, $V_{oc} = 0.65 \text{ eV}$, $I_{sc} = 9 \text{ mA}$, $V_{oc} = 0.65 \text{ eV}$, $I_{sc} = 10 \text{ mA}$ and $V_{oc} = 0.7 \text{ eV}$, $I_{sc} = 10 \text{ mA}$ (considering the ideality factor $\eta = 1.5$).

The potential barrier values required to obtain the solar cells with the above characteristics were calculated: 1.171 eV ($V_{oc} = 0.65 \text{ eV}$, $I_{sc} = 8 \text{ mA}$), 1.168 eV ($V_{oc} = 0.65 \text{ eV}$, $I_{sc} = 9 \text{ mA}$), 1.166 eV ($V_{oc} = 0.65 \text{ eV}$,

$I_{sc} = 10 \text{ mA}$) and 1.199 eV ($V_{oc} = 0.7 \text{ eV}$, $I_{sc} = 10 \text{ mA}$). In addition, we also determine the values referring to the PCE: 21.41%, 24.09%, 26.76% and 29.23%, respectively.

For elaboration of Fig. 12, we use Eqs. 15, 27, 30 and $\phi_B = \frac{k_B T}{q} \ln \left(\frac{AA^* T^2}{I_0} \right)$.

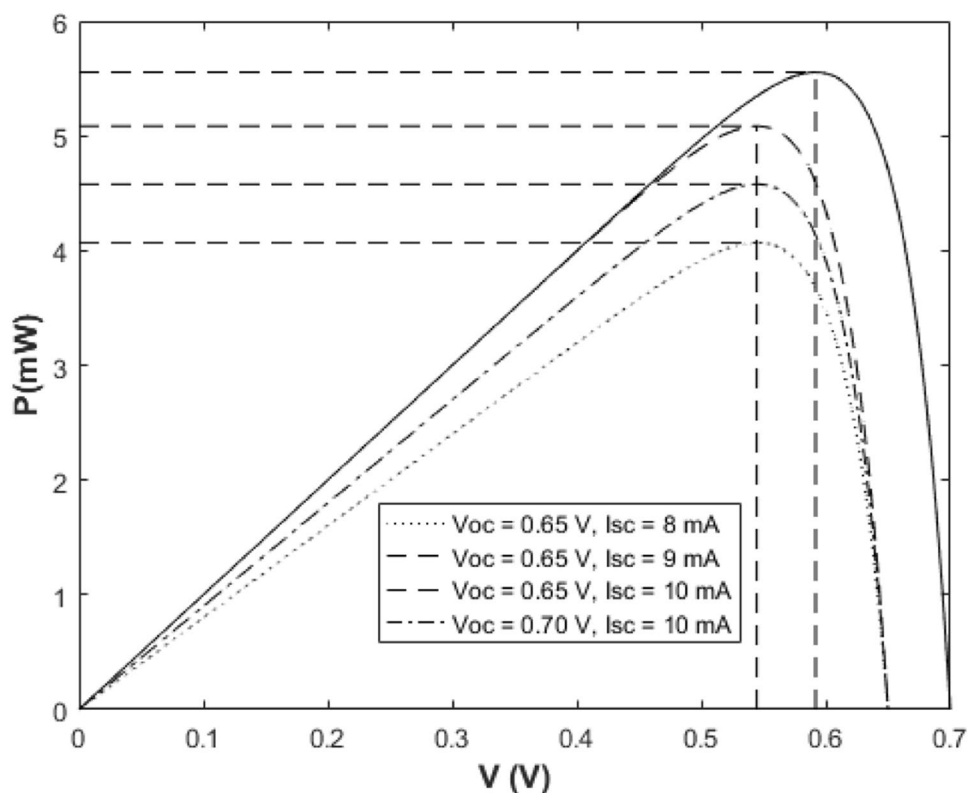
We believe the information may be used in researches referring to this type of solar cell.

6 Molybdenum disulfide (MoS_2 —molybdenite)

6.1 Overview

Like graphite, there are many other types of crystals, called transition metal dichalcogenides, such as, for example, MoS_2 , MoSe_2 , WS_2 , WSe_2 and their oxides, which have atomic structure with strong bonds between atoms located in the same layer, but with weak interactions (van der Waals type) between these layers. These materials can be easily exfoliated, a single layer being called 2D material. Due to their excellent electro-electronic properties, the transition metal dichalcogenides (TMDCs) are being researched all over the world. TMDCs have MX_2 formula, where M is a transition metal element belonging to group IV (Ti, Zr, Hf), group V (V, Nb, Ta), or group VI (Mo, W) of the periodic

Fig. 12 Graphs (V, P) referring to solar cells with the following parameters: $V_{oc} = 0.65 \text{ eV}$, $I_{sc} = 8 \text{ mA}$, $V_{oc} = 0.65 \text{ eV}$, $I_{sc} = 9 \text{ mA}$, $V_{oc} = 0.65 \text{ eV}$, $I_{sc} = 10 \text{ mA}$ and $V_{oc} = 0.7 \text{ eV}$, $I_{sc} = 10 \text{ mA}$



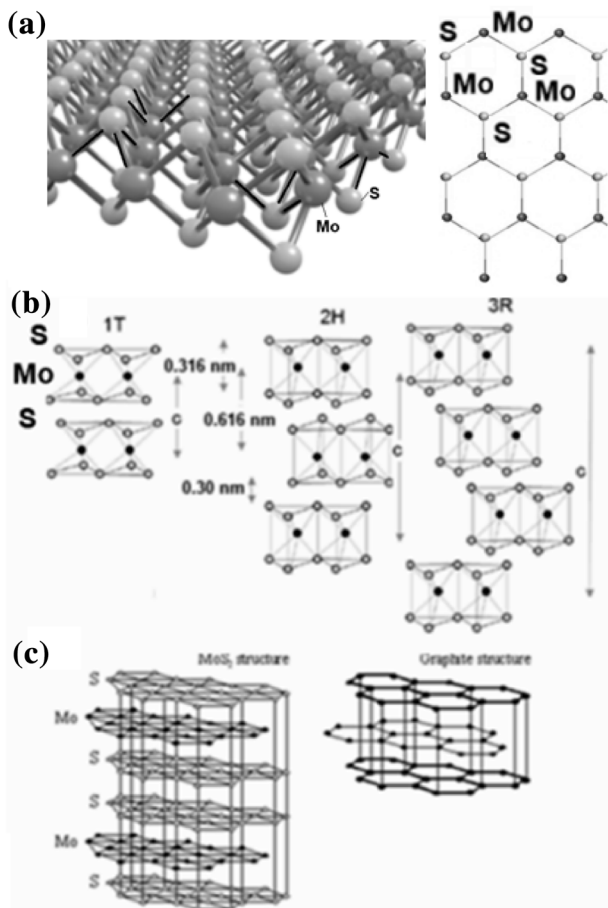


Fig. 13 **a** Atomic structure referring to the atoms of the MoS₂ layer. **b** Schematic representations of the types of primitive cells (adapted, with permission of Ref. [40]). **c** Comparison between crystal structures of graphite and MoS₂

table and X is a chalcogen (S, Se, Te—element belonging to group XVI (VI A)).

As shown in the left part of Fig. 13a, the TMDCs are made up of layered structures of form X–M–X, so that a layer of TMDC is constituted by two layers (planes) of chalcogen atoms and between these two planes is embedded a plane constituted by transition metal atoms.

As we can see in the right part of Fig. 13a, the top view (and back view) of the bonded atoms presents a hexagonal structure. Indeed, a layer of 2D MoS₂, for example, is formed by three layers, the Mo atoms layer being embedded between two layers of S atoms.

Note that each Mo atom is located in the center of a trigonal prismatic structure consisting of six S atoms located at the vertices (unit Mo(S)₆). On the other hand, each sulfur atom is located at the apex of a pyramid, which is connected to three Mo atoms located at the base of this pyramid (Fig. 13a).

It is noteworthy that MoS₂ has strong intra-layer covalent bonds, but inter-layer bonds are formed by weak van de Waals interactions (vdW) between the adjacent layers, i.e., all ligand orbitals relating to silicon and molybdenum atoms are completely involved in intra-layer bonds and there are only high-energy anti-ligand orbitals available for the interlayer bonds.

MoS₂ can present three different polytypes of crystalline structure (1T, 2H, and 3R). In the nomenclature of MoS₂ polytypes, the number indicates the number of layers existing within a single crystallographic unit cell, and the letter represents the crystallographic structure, where T stands for trigonal structure, H hexagonal structure, and R rhombohedral structure, as shown in Fig. 13b [40]. It is worth noting that the structures named 2H and 3R are stable and found in nature [41]. Note that 2H type has a primitive cell using two S–Mo–S layers and that 3R type uses three S–Mo–S layers for the formation of a primitive cell. These two polytypes generally have Mo atoms with trigonal prismatic coordination, but with different orders of stacking with respect to the layers of sulfur atoms and share the crystallographic parameters.

The distance between an Mo atom and the adjacent S atom is 0.241 nm [42, 43] and the layer thickness is 0.315 nm.

On the other hand, the 1T type was discovered in the decade referring to the 1990s, has octahedral atomic coordination of Mo atoms and is metastable, metallic and paramagnetic [44–46]. This type of structure is obtained through synthesis, via hydration and oxidation, and has only one layer of MoS₂ in the formation of a unit cell, according to its nomenclature. It is noteworthy that the atomic structures types 1T and 3R of MoS₂ can be changed to type 2H by annealing [47, 48].

Figure 13c shows the comparison between the crystal structures of graphite and MoS₂.

6.2 Characteristics of 2H (2H-MoS₂) and 3R (3R-MoS₂) polytypes with trigonal prismatic coordination and 1T (1T-MoS₂) with octahedral coordination

Analyzing the structure of energy bands related to 2H-MoS₂, it is possible to state that the wave number referring to the maximum valence band (VBM) is different from the wave number that corresponds to the minimum value of the conduction band (CBM) so that this polytype presents indirect bandgap [49]. Therefore, the 2H-MoS₂ found in nature is a diamagnetic semiconductor with an indirect bandgap, whose value is 1.29 eV [50, 51]. The 2H-MoS₂ absorption spectrum has two peaks: for photons with energy 1.9 eV ($\lambda \approx 640$ nm) and 2.1 eV ($\lambda \approx 580$ nm) [52, 53]. With respect to the transport of charges, previous research has shown that

this polytype behaves as a semiconductor, having a charge mobility value of $100 \text{ cm}^2 \text{ V}^{-1} \text{ s}^{-1}$ at room temperature [54]. Moreover, 2H-MoS₂ is totally chemically inert at room temperature and in the vacuum is stable up to 1203 °C, and at this temperature, it becomes Mo₂S₃ [55]. At temperatures between 400 and 600 °C, the 2H-MoS₂ reacts with oxygen, forming MoO₃ [49].

The physical and chemical properties of the 3R-MoS₂ polymorph are substantially identical to those of the 2H-MoS₂ polytype.

Most of the natural molybdenite is of the 2H-MoS₂ type (80%) and only 3% is of the 3R-MoS₂ type, the remainder being present in mixtures [56]. It is noteworthy that large volumes of these polytypes can be obtained artificially through chemical synthesis, most often by the chemical vapor transport (CVT) method, through annealing at high temperatures for several days of the mixture of Mo, S and halogen iodine for 2H-MoS₂, as well as chlorine for 3R-MoS₂ [54, 57].

Unlike the polymorphs 2H-MoS₂ and 3R-MoS₂, the 1T-MoS₂ polytype is metal metastable and paramagnetic, due to the octahedral coordination of Mo atoms [44–46]. Research has shown that there are three types of superstructures for the 1T-MoS₂ polytype ($2a \times 2a$, $\sqrt{3}a \times a$ and $\sqrt{3}a \times \sqrt{3}a$), depending on the intensity of the oxidation used during the manufacturing process [45, 58–61]. It is worth noting that the polytype with superstructure $\sqrt{3}a \times \sqrt{3}a$ has a small bandgap and presents greater instability [56]. Complementing, by the annealing of 1T-MoS₂ up to the temperature of 95 °C, this polytype is transformed into 2H-MoS₂.

6.3 Energy band structure and charge carrier transport

One of the advantages of 2D MoS₂ is its behavior as a semiconductor. Through previous studies, it has been proven that the 2D 2H-MoS₂ presents direct bandgap with a value of 1.9 eV. Graphene, for example, behaves like a semimetal, the opening of a bandgap in this material being a very complicated process. However, this bandgap may undergo change with the application of a voltage, so that in this case the said bandgap is again of the indirect type [62–64]. On the other

hand, 2D 1T-MoS₂ with superstructure $\sqrt{3}a \times \sqrt{3}a$ presents bandgap with a value of 0.7 eV [65].

Research has shown that in a typical field-effect transistor (FET) with 2D molybdenite channel, application of back gate causes MoS₂ to behave as an n-type semiconductor, with load mobility of $0.5 \text{ cm}^2 \text{ V}^{-1} \text{ s}^{-1}$ in ambient temperature [66]. In addition, inserting of a dielectric material with a high dielectric constant (such as HfO₂), i.e., the use of a top gate, can increase the value of the MoS₂ charge motility [67, 68]. It is worth noting that this effect is also valid for the channel consisting of a few layers of MoS₂ so that despite indirect bandgap, few MoS₂ layers still have semiconductor characteristics [69].

Another way to modulate the electrical properties of these types of semiconductors is the use of chemical doping. However, to achieve good results, a density of carrier charges with a minimum value of $5 \times 10^{11} \text{ cm}^{-2}$ is necessary [70]. Higher doping values using Nb make MoS₂ as a p-type semiconductor, with charge mobility $8.5 \text{ cm}^2 \text{ V}^{-1} \text{ s}^{-1}$ [71]. On the other hand, to obtain MoS₂ with n-type semiconductor characteristics, alkali metal vapor, such as potassium (K), can be used, so that we can reach density of carrier charges up to $1 \times 10^{13} \text{ cm}^{-2}$ [72, 73].

Complementing the basic information regarding this subject, a moderate level of doping via gate voltage induces the doping effect as in typical semiconductors. However, a higher level of doping, with a density of charge carriers greater than $1 \times 10^{13} \text{ cm}^{-2}$, induces the semiconductor transition to metal due to electron–electron interactions [74].

6.4 Absorption and emission characteristics for 2D MoS₂

Previous research has revealed the absorption spectrum for a 2D MoS₂ layer, as well as showed and explained some discrepancies between the respective results [50, 75, 76], as shown in Table 1 (five first peaks of absorbance, for photon energy between 1.5 and 3.5 eV).

The calculation methodology in Ref. [75] has taken into account that the absorption spectrum is provided by exciton states (referring to quasi-particles) and electron–phonon interactions, in the energy band of photons between the visible region and the ultraviolet region. This calculation methodology was based, firstly, on the DFT methodology

Table 1 Absorbance peaks (A, B, C, D, E, F) as a function of the energy of the incident photon

Reference	Photon energy (eV)					Absorbance (%)				
	A	B	C	D	E	A	B	C	D	E
75A	1.88	2.02	2.20	2.32	2.54	≈ 11.32	≈ 12.45	≈ 18.11	≈ 19.25	≈ 60
75B	1.88	2.02			≈ 2.90	≈ 8.30	≈ 10.57			≈ 23.40
76	1.88	2.03			≈ 2.90	≈ 10.57	≈ 10.57			≈ 35.47
77	1.78	1.96	≈ 2.84	≈ 3.03	≈ 3.32					

admitting the local density approximation (LDA). Then, the GW calculation methodology (G represents “green function” and W stands for “dynamic screened interaction potential”) was applied, which determined the direct bandgap with a value equal to 2.84 eV. After obtaining the above result, the absorption spectrum of 2D MoS₂ 2D (75(A)) was determined, and it was proved that for photon energy above 2 eV, convergent calculations with more points in the k grid are needed. In addition, it has been shown that changes occur between the absorbance spectrum (75(A)) and presented through experiments (76) because it is necessary to take into account the electron–phonon interactions. It has been shown that the scattering rate of quasiparticles in MoS₂ due to electron–phonon interactions is highly dependent on the energies of these quasiparticles, and in the existence of almost all electrons with sufficient energy to emit an optical phonon (50 meV), an increase in absorbance values occurs [77]. Taking into account what was mentioned above, the results were obtained following the methodology presented in another research [78], which are shown in Table 1(75B), whose results are similar to those presented on a previous obtained experimental basis.

7 Technical detail regarding MoS₂-based solar cells

Heterostructures can be defined as the stacking of two or more thin films (or 2D films) made up of different materials, where the energy bands structures of the involved materials interact at the interfaces. Therefore, it is possible to use this interaction of energy bands to obtain control of the charge carriers located in these interfaces [79].

Photovoltaic devices consisting of p–n junctions based on WSe₂/MoS₂ were studied. The results of these studies showed that these devices presented external quantum efficiency (EQE) of 10–30% for different thicknesses [80, 81].

Currently, mechanical assembly (using solvent-assistant method [82] and all-dry transfer technique [83]), and chemical vapor deposition (CVD)/epitaxy [80, 84] are the two most commonly used approaches for obtaining van der Waals heterojunctions. It is worth mentioning that while the mechanical assembly method provides devices with high efficiency, the CVD/epitaxy method provides large-scale heterostructures with very well controlled orientations among the layers [79].

A solar cell consisting of n-MoS₂/i-SiO₂/p-Si was fabricated and studied [85]. Considering the inclusion of a nano-scale SiO₂ buffer, the above-mentioned solar cell presented a PCE of 4.5%. This solar cell was obtained by depositing the thin bulk film of MoS₂ on the SiO₂ layer located above the p-type Si substrate, i.e., the SiO₂ layer is embedded

between the thin film of MoS₂ and the p-type Si substrate. The SiO₂ layer has three utilities: (1) its low interface state density with $1 \times 10^{10} \text{ cm}^{-2} \text{ eV}$, which was achieved through the use of high temperature under oxidizing atmosphere during SiO₂ generation [86, 87]; (2) obtaining an MoS₂ uniform monolayer film with a relatively great size due to the use of SiO₂/Si as the substrate [88, 89]; (3) taking into account that the SiO₂ layer is an insulating buffer, the amount of recombination near the interface is decreased, which improves the photovoltaic properties of this solar cell [90].

The results of the research related to this solar cell showed that its efficiency increases greatly when the nano-scale SiO₂ buffer is inserted between the layers of MoS₂ and p-Si. It is worth noting that the energy-band structure near the interface was used to demonstrate the increased effectiveness referred to the solar cell mentioned above [85].

Obtaining a single and few layers of MoS₂ led to the elaboration of studies related to the solar cells constituted by heterojunctions based on MoS₂, due to the great optical absorption in the range of wavelengths of sunlight, fast optical response, low cost and chemical stability of ultrafine MoS₂ layers [91–93].

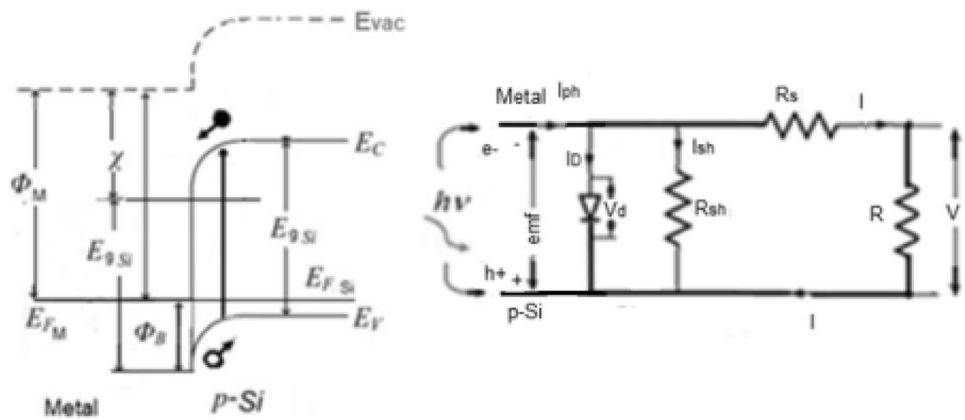
Solar cells constituted by n-MoS₂/p-Si heterojunctions were analyzed by the “Analysis of Microelectronic and Photonic Structures (AMPS 1D)” software, so that the effects on the efficiency of these solar cells due to the bandgap, electron affinity, thickness of the MoS₂ layer, and concentration of donors in silicon were simulated and analyzed in detail. Additionally, the effects caused by defects of energy states in the silicon layer, as well as in the n-MoS₂/p-Si interface were also considered.

Taking into account the control of the inherent defects to the interface, since these defects influence the performance of this type of solar cell, these studies revealed that solar cells constituted by 2D MoS₂, which has bandgap of 1.8 eV, forming a heterojunction with highly doped p-Si have a conversion efficiency above 19% [94].

To carry out the simulations regarding these solar cells, the standard illumination spectrum (AM1.5) was used and the values referring to the absorption coefficient of 2D MoS₂ obtained from other studies [95] were taken into account. For the simulations, it was considered that the recombination velocity for electrons and holes on the surface has a value of $1 \times 10^7 \text{ cm}^{-1}$ and the reflections occurring on the front and lower surfaces were neglected.

To obtain sufficient amount of photons absorption, the thicknesses of the MoS₂ film and the silicon layer were 10 nm and 200 μm , respectively, and the donor (N_D) and acceptor (N_A) concentrations were set to the moderate value of $1 \times 10^{17} \text{ cm}^{-3}$. The thickness of the silicon layer was determined to achieve sufficient light absorption, since the absorbance relative to the small thickness of the MoS₂ film is negligible.

Fig. 14 Left part: diagram of typical energy bands referring to a metal/p-Si Schottky junction. Right part: equivalent electrical circuit relative to a solar cell based on metal/p-semiconductor Schottky junction



Considering that electron affinity value of MoS₂ is in the range of 4.0 to 4.7 eV and bandgap between 1.2 eV (bulk) and 1.8 eV (monolayer), the results showed the effects in the efficiency of those solar cells, due to the variations in the values mentioned above. To understand the reasons for what was mentioned above about solar cells with n-MoS₂/p-Si junction, we first show what would be the behavior regarding a metal/p-Si solar cell, as can be seen in Fig. 14.

As shown in the left-hand part of Fig. 14, also in this case, the embedded electric field has an inverse direction to that occurring in metal/n-semiconductor junctions. This field separates the charge carriers so that the electrons are directed to the metal and holes to the p-semiconductor. Note that the metal Fermi level remains constant (due to the high value of charge density), unlike what occurs in the n-MoS₂/p-Si junction, where the Fermi level for n-MoS₂ also undergoes displacement as a function of the value of the doping and of its band gap (E_g), as we will see below.

Recall that in this case, the potential barrier is given by $\Phi_B = E_{gSi} - (\Phi_M - \chi_{Si})$ and the built-in potential is given by $\Phi_i = \Phi_B - |E_F - E_V|$.

Through the right part of this figure we can also notice that in this case, the external electric current has an opposite direction with respect to the external current occurring in metal/n-semiconductor Schottky junction, that is, the electron current in the external circuit is directed away from the metal and toward the p-semiconductor.

On the other hand, for the n-MoS₂/p-Si heterojunction, we must replace the metal work function with the MoS₂ electron affinity. However, the change of the value of the work function and/or of the value of the bandgap of MoS₂ (E_{gMoS_2}) changes the position of the Fermi level of the device.

It has been demonstrated in the simulations mentioned above that the value of V_{oc} increases with the increase of the bandgap value between 1.2 and 1.5 eV, but between 1.5 and 1.8 eV, the value of V_{oc} remains approximately constant. In addition, in this bandgap range, the increase in the

electron affinity value of MoS₂ (between 4.0 and 4.7 eV) causes only a small decrease in the value of V_{oc} which has an average value of 0.675 eV. Moreover, with increase in the bandgap value, the current density value remains practically constant, but decreases from approximately 34.5 mA/cm² ($\chi_{Mo} = 4.0$ eV; $E_g = 1.8$ eV) to approximately 33.5 mA/cm² ($\chi_{Mo} = 4.7$ eV; $E_g = 1.2$ eV). The value of the conversion efficiency varies from $\eta \approx 11.5\%$ ($\chi_{Mo} = 4.7$ eV; $E_g = 1.2$ eV) to $\eta = 19.37\%$ ($\chi_{Mo} = 4.0$ eV; $E_g = 1.8$ eV).

One of the explanations about what was detailed above is the change in the level of the conduction band near the interface, since for $\chi_{Mo} = 4.0$ eV the influence of the built-in field increases, so that an improvement regarding the separation and charge transport occurs. On the other hand, for $\chi_{Mo} = 4.7$ eV the inverse with respect to the built-in electric field occurs, and in this case, a degradation regarding the process of separation and transport of charge arises.

Indeed, p-silicon has its Fermi level shifted down in relation to the Fermi level of the intrinsic silicon (considered as located in the middle of its bandgap), the value of this displacement being given by:

$$\Delta E_F = K_B T \ln \left(\frac{N_A}{n_i} \right). \quad (35)$$

Hence, considering the intrinsic charge of silicon $n_{iSi} = 1.45 \times 10^{10} \text{ cm}^{-3}$, the value of the displacement of the silicon Fermi level is $\Delta E_F = 0.47$ eV (downward). Therefore, $E_0 - E_F \approx 5.08$ eV, as it can be observed in the left part of Fig. 15 (theoretical energy band structures referring to isolated n-MoS₂ and p-Si).

Since the concentration of intrinsic carriers in the 2D MoS₂ is very low ($n_{iMo} \approx 1.1 \times 10^{-2} \text{ cm}^{-2}$, which is much smaller than that of graphene $n_{iG} \approx 10^{11} \text{ cm}^{-2}$ [96]), its Fermi level, in this case, is located very close to its conduction band.

Considering $\chi_{Si} = 4.05$ eV [97], $\chi_{Mo} = 4.0$ eV, $E_g = 1.12$ eV, and $T = 300$ K, we have that the

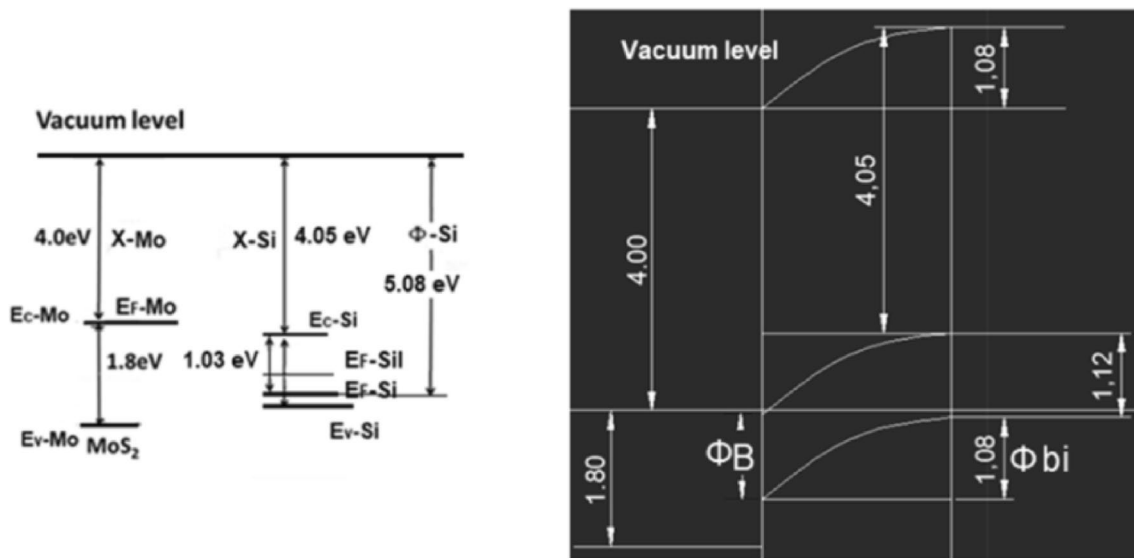


Fig. 15 Left part: theoretical energy band diagrams referring to isolated MoS₂ and Si. Right part: theoretical energy band diagrams referring to the n-MoS₂/p-Si junction

built-in potential is $\Phi_{\text{bi}} = \Phi_{\text{Si}} - \Phi_{\text{Mo}} = 1.08 \text{ eV}$, and $\Delta E_{\text{c}} = \chi_{\text{Si}} - \chi_{\text{Mo}} = 0.05 \text{ eV}$; $\Delta E_{\text{v}} = (\chi_{\text{Mo}} + E_{\text{gMo}}) - (\chi_{\text{Si}} + E_{\text{gSi}}) = 0.63 \text{ eV}$.

Observe in the right part of Fig. 15 that in the energy bandwidth diagram for the n-MoS₂/p-Si heterojunction, the value of the potential barrier is $\Phi_{\text{B}} = E_{\text{gMo}} - \Delta E_{\text{v}} = 1.17 \text{ eV}$.

It is noteworthy that the simulations referring to the real device [94] presented some changes in relation to the theoretical energy band structures presented in this figure. However, these changes do not significantly alter the theoretical results we have found.

Using Eq. 27 ($I_0 = \frac{I_{\text{sc}}}{\left(\frac{qV_{\text{oc}}}{\eta k_{\text{B}}T} \right)}$), we determined the value $I_0 \approx 5.55 \times 10^{-18} \text{ A}$, considering the ideal Schottky junction (ideality factor $\eta = 1$), for $J_{\text{sc}} = 34.5 \text{ mA/cm}^2$, $V_{\text{oc}} = 0.66 \text{ eV}$, and effective contact area 0.19 cm^2 .

Note that the value of I_{sc} (short-circuit current) depends on the value of I_0 (reverse current), which in turn depends on the value of the potential barrier (ϕ_{B}).

Note also, through Eq. 2 ($I_0(T) = AA^*T^2 e^{-\frac{\Phi_{\text{B}}}{k_{\text{B}}T}}$) that the larger the value of ϕ_{B} , the smaller is the value of I_0 . It is noteworthy that the value of I_0 determined by this equation is $4.24 \times 10^{-14} \text{ A}$. Then we find numerically the value of the ideality factor $\eta \approx 1.56$ through Eq. 27, varying the value of η until we find the same value of I_0 ($4.24 \times 10^{-14} \text{ A}$). It is worth noting that since the value of the Richardson constant (A^*) is not perfectly determined for silicon in contact with MoS₂, the value of η can be altered by changing the value of A^* .

Complementing, since V_{oc} depends on the Neperian logarithm of $\frac{I_{\text{sc}}}{I_0}$ (according to Eq. 17, i.e., $V_{\text{oc}} \approx \frac{\eta k_{\text{B}}T}{q} \ln \left(\frac{I_{\text{ph}}}{I_0} \right)$), its variation is small.

8 Conclusions

We presented a detailed review of the solar cells based on graphene/silicon Schottky junction and on MoS₂/silicon heterojunction. For a better understanding of the technology used in the solar cells mentioned above, before we detail these solar cells, we initially showed the graphene/semiconductor Schottky junction, as well as the adaptation of the thermionic theory to this type of junction. Then, after the steps mentioned above, we showed the solar cells constituted by graphene/silicon Schottky junction. Since monolayer (or few layers) of MoS₂ are used in solar cells, we detailed the theory involving this material. This review is completed with the presentation of solar cells constituted by the MoS₂/silicon heterojunction.

Acknowledgements This work was partly sponsored by the Cearense Foundation for Scientific and Technological Development Support (FUNCAP) (Grant no. DCR-0024-00026.03.00/14) and National Council for Scientific and Technological Development (CNPq) (Grant no. 314915/2018-4).

References

1. Y. Wu, X. Zhang, J. Jie, C. Xie, X. Zhang, B. Sun, Y. Wang, P. Gao, Graphene transparent conductive electrodes for highly efficient silicon nanostructures-based hybrid heterojunction solar cells. *J. Phys. Chem. C* **117**, 11968–11976 (2013)
2. J. Li-Li, L. Xiong, Graphene applications in solar cells. *J. Inorg.* **27**, 1129–1137 (2012)
3. X.S. Li, Y.W. Zhu, W.W. Cai, M. Borysiak, B.Y. Han, D. Chen, R.D. Piner, L. Colombo, R.S. Ruoff, Transfer of large-area graphene films for high-performance transparent conductive electrodes. *Nano Lett.* **9**, 4359–4363 (2009)
4. B. Radisavljevic, A. Radenovic, J. Brivio, V. Giacometti, A. Kis, *Nat. Nanotechnol.* **6**, 147 (2011)
5. M. Bernardi, M. Palummo, J.C. Grossman, Extraordinary sunlight absorption and one nanometer thick photovoltaics using two-dimensional monolayer materials. *Nano Lett.* **13**, 3664–3670 (2013)
6. R.R. Nair, P. Blake, A.N. Grigorenko, K.S. Novoselov, T.J. Booth, T. Stauber, N.M.R. Peres, A.K. Geim, Fine structure constant defines visual transparency of graphene. *Science* **320**, 1308 (2008)
7. A. Di Bartolomeo, *Graphene Schottky Diodes: An Experimental Review of the Rectifying Graphene/Semiconductor Heterojunction* (Elsevier, Amsterdam, 2015). <https://doi.org/10.1016/j.physrep.2015.10.003>
8. L.A. Falkovsky, S.S. Pershoguba, Optical far-infrared properties of a graphene monolayer and multilayer. *Phys. Rev. B* **76**, 153410 (2007)
9. J. Christensen, A. Manjavacas, S. Thongrattanasiri, F.H.L. Koppens, F.J.G. de Abajo, Graphene plasmon waveguiding and hybridization in individual and paired nanoribbons. *Am. Chem. Soc.* **6**(1), 431–440 (2012)
10. J.S. Oh, K.N. Kim, G.Y. Yeom, Graphene doping methods and device applications. *J. Nanosci. Nanotechnol.* **14**, 1120–1133 (2014)
11. T.S. Abhilash, R. De Alba, N. Zhelev, H.G. Craighead, J.M. Parpia, Transfer printing of CVD graphene FETs on patterned substrates. *Nanoscale* **7**, 14109–14113 (2015)
12. S.J. Liang, W. Hu, A. Di Bartolomeo, S. Adam, L.K. Ang, A modified Schottky model for graphene-semiconductor (3D/2D) contact: a combined theoretical and experimental study, in *IEEE International Electron Devices Meeting (IEDM)* (2016). <https://doi.org/10.1109/IEDM.2016.7838416> (ISSN: 2156-017X)
13. S.J. Liang, L.K. Ang, Electron thermionic emission from graphene and a thermionic energy converter. *Phys. Rev. Appl.* **3**, 014002–014010 (2015)
14. A. Di Bartolomeo, F. Giubileo, G. Luongo, L. Iemmo, N. Martucciello, G. Niu, M. Frascake, O. Skibitzki, T. Schroeder, G. Lupina, Tunable Schottky barrier and high responsivity in graphene/Si-nanotip optoelectronic device. *2D Mater.* **4**, 015024 (2017)
15. F.A. Chaves, D. Jiménez, A.W. Cummings, S. Roch, Physical model of the contact resistivity of metal–graphene junctions. *J. Appl. Phys.* **115**, 164513 (2014)
16. D. Tomer, S. Rajput, L.J. Hudy, C.H. Li, L. Li, *Inhomogeneity in Barrier Height at Graphene/Si (GaAs) Schottky Junctions*, vol 26(21) (IOP Publishing Ltd Nanotechnology, Bristol, 2015)
17. S.M. Sze, K.K. Ng, *Physics of Semiconductor Devices*, 3rd edn. (Wiley, Hoboken, 2006)
18. L. Castañer, S. Silvestre, *Modelling Photovoltaic Systems Using PSpice* (Wiley, Hoboken, 2002)
19. X. Li, H. Zhu, K. Wang, A. Cao, J. Wei, C. Li, Y. Jia, Z. Li, X. Li, D. Wu, Graphene-on-silicon schottky junction solar cells. *Adv. Mater.* **22**, 2743–2748 (2010)
20. P. Neugebauer, M. Orlita, C. Faugeras, A.L. Barra, M. Potemski, *Phys. Rev. Lett.* **103**, 136403 (2009)
21. Y. Lin, X. Li, D. Xie, T. Feng, Y. Chen, R. Song, H. Tian, T. Ren, M. Zhong, K. Wangb, H. Zhu, Graphene/semiconductor heterojunction solar cells with modulated antireflection and graphene work function. *Energy Environ. Sci.* **6**, 108–115 (2013)
22. H.K. Jeong, K.-J. Kim, S.M. Kim, Y.H. Lee, Modification of the electronic structure of graphene by viologen. *Chem. Phys. Lett.* **498**, 168–171 (2010)
23. Y. Yi, W.M. Choi, Y.H. Kim, J.W. Kim, S.J. Kang, Effective work function lowering of multilayer graphene films by sub-nanometer thick AlO_x overlayers. *Appl. Phys. Lett.* **98**, 013505 (2011)
24. Y. Shi, K.K. Kim, A. Reina, M. Hofmann, L.-J. Li, J. Kong, Work function engineering of graphene electrode via chemical doping. *ACS Nano* **4**, 2689–2694 (2010)
25. C.-H. Sun, P. Jiang, B. Jiang, Broadband moth-eye antireflection coatings on silicon. *Appl. Phys. Lett.* **92**, 061112 (2008)
26. K.K. Kim, A. Reina, Y. Shi, H. Park, L.-J. Li, Y.H. Lee, J. Kong, Enhancing the conductivity of transparent graphene films via doping. *Nanotechnology* **21**, 285205 (2010)
27. A. Suhail, G. Pan, D. Jenkins, K. Islam, Improved efficiency of graphene/Si Schottky junction solar cell based on back contact structure and DUV treatment. *Carbon* **129**, 520–526 (2018)
28. Y. Song, X. Li, C. Mackin, X. Zhang, W. Fang, T.s. Palacios, H. Zhu, J. Kong, Role of interfacial oxide in high-efficiency graphene–silicon Schottky barrier solar cells. *Nano Lett.* **15**(3), 2104–2110 (2015)
29. A.G. Aberle, Surface passivation of crystalline silicon solar cells: a review. *Prog. Photovolt. Res. Appl.* **8**(5), 473–487 (2000)
30. B.-S. Wu, Y.-C. Lai, Y.-H. Cheng, S.-C. Yu, P. Yu, G.-C. Chi, Hybrid multi-layer graphene/Si Schottky junction solar cells, in *Photovoltaic Specialists Conference (PVSC), IEEE 39th* (IEEE, New York, 2013), pp. 2486–2489
31. A. Suhail, K. Islam, B. Li, D. Jenkins, G. Pan, Reduction of polymer residue on wet-transferred CVD graphene surface by deep UV exposure. *Appl. Phys. Lett.* **110**(18), 183103 (2017)
32. Y. Wang, C. Chen, X. Fang, Z. Li, H. Qiao, B. Sun, Q. Bao, Top-grid monolayer graphene/Si Schottkey solar cell. *J. Solid State Chem.* **224**, 102–106 (2015)
33. Y. Xu, C. Cheng, S. Du, J. Yang, B. Yu, J. Luo, W. Yin, E. Li, S. Dong, P. Ye, Contacts between two-and three-dimensional materials: ohmic, Schottky, and p-n heterojunctions. *ACS Nano* **10**(5), 4895–4919 (2016)
34. X. Miao, S. Tongay, M.K. Petterson, K. Berke, A.G. Rinzier, B.R. Appleton, A.F. Hebard, High efficiency graphene solar cells by chemical doping. *Nano Lett.* **12**(6), 2745–2750 (2012)
35. Y. Choi, J. Lee, J. Seo, S. Jung, U. Kim, H. Park, The effect of the graphene integration process on the performance of graphene-based Schottky junction solar cells. *J. Mater. Chem.* **5**(35), 18716–18724 (2017)
36. J.W. Suk, W.H. Lee, J. Lee, H. Chou, R.D. Piner, Y. Hao, D. Akinwande, R.S. Ruoff, Enhancement of the electrical properties of graphene grown by chemical vapor deposition via controlling the effects of polymer residue. *Nano Lett.* **13**(4), 1462–1467 (2013)
37. K.S. Kim, Y. Zhao, H. Jang, S.Y. Lee, J.M. Kim, K.S. Kim, J.-H. Ahn, P. Kim, J.-Y. Choi, B.H. Hong, Large-scale pattern growth of graphene films for stretchable transparent electrodes. *Nature* **457**(7230), 706–710 (2009)
38. T. Cui, R. Lv, Z.-H. Huang, S. Chen, Z. Zhang, X. Gan, Y. Jia, X. Li, K. Wang, D. Wu, Enhanced efficiency of graphene/silicon heterojunction solar cells by molecular doping. *J. Mater. Chem.* **1**(18), 5736–5740 (2013)
39. E. Singh, H.S. Nalwa, Stability of graphene-based heterojunction solar cells. *RSC Adv.* **5**(90), 73575–73600 (2015)
40. M. Ye, D. Winslow, D. Zhang, R. Pandey, Y.K. Yap, Recent advancement on the optical properties of two-dimensional

- molybdenum disulfide (MoS₂) thin films. *Photonics* **2**, 288–307 (2015). <https://doi.org/10.3390/photonics2010288>
41. P. Jelinek, G. Brauer, H. Müller, Molybdenum and niobium sulphides. *Nature* **185**, 185376–185377 (1960)
 42. G.A. Tsigdinos, *Aspects of Molybdenum and Related Chemistry*, vol. 76 (Springer, Berlin, 1978), pp. 65–105
 43. R.G. Dickinson, L. Pauling, *J. Am. Chem. Soc.* **45**, 1466–1471 (1923)
 44. F. Wypych, R. Schöllhorn, *J. Chem. Soc., Chem. Commun.* 1386–1388 (1992)
 45. F. Wypych, T. Weber, R. Prins, *Chem. Mater.* **10**, 723–727 (1998)
 46. F. Wypych, K. Sollmann, R. Schöllhorn, *Mater. Res. Bull.* **27**, 545–553 (1992)
 47. A.N. Enyashin, L. Yadgarov, L. Houben, I. Popov, M. Weidenbach, R. Tenne, M. Bar-Sadan, G. Seifert, New route for stabilization of 1T-WS₂ and MoS₂ phases. *J. Phys. Chem. C* **115**, 24586–24591 (2011)
 48. G. Eda, H. Yamaguchi, D. Voiry, T. Fujita, M. Chen, M. Chhowalla, Photoluminescence from chemically exfoliated MoS₂. *Nano Lett.* **11**, 5111–5116 (2011)
 49. I. Song, C. Parkab, H.C. Choi, Synthesis and properties of molybdenum disulphide: from bulk to atomic layers. *RSC Adv.* **5**, 7495 (2015)
 50. K.F. Mak, C. Lee, J. Hone, J. Shan, T.F. Heinz, *Phys. Rev. Lett.* **105**, 136805 (2010)
 51. R.V. Kasowski, *Phys. Rev. Lett.* **30**, 1175–1178 (1973)
 52. A. Clark, R.H. Williams, *J. Phys. D Appl. Phys.* **1**, 1222–1224 (1968)
 53. R. Suzuki, M. Sakano, Y.J. Zhang, R. Akashi, D. Morikawa, A. Harasawa, K. Yaji, K. Kuroda, K. Miyamoto, T. Okuda, K. Ishizaka, R. Arita, Y. Iwasa, *Nat. Nanotechnol.* **9**, 611–617 (2014)
 54. R. Fivaz, E. Mooser, *Phys. Rev.* **163**, 743–755 (1967)
 55. D. Liu, X. Chen, D. Li, F. Wang, X. Luo, B. Yang, *J. Mol. Struct.* **980**, 66–71 (2010)
 56. J.W. Frondel, F.E. Wickman, *Am. Mineral.* **55**, 1857–1875 (1970)
 57. W. Koehler, US Patent 1,714,564 (1929)
 58. P.J. Mulhern, *Can. J. Phys.* **67**, 1049–1052 (1989)
 59. D. Yang, S. Sandoval, W. Divigalpitiya, J. Irwin, R. Frindt, *Phys. Rev. B Condens. Matter Mater. Phys.* **43**, 12053–12056 (1991)
 60. K.E. Dungey, M.D. Curtis, J.E. Penner-Hahn, *Chem. Mater.* **10**, 2152–2161 (1998)
 61. J. Heising, M.G. Kanatzidis, *J. Am. Chem. Soc.* **121**, 11720–11732 (1999)
 62. C.R. Zhu, G. Wang, B.L. Liu, X. Marie, X.F. Qiao, X. Zhang, X.X. Wu, H. Fan, P.H. Tan, T. Amand, B. Urbaszek, *Phys. Rev. B Condens. Matter Mater. Phys.* **88**, 121301 (2013)
 63. H.J. Conley, B. Wang, J.I. Ziegler, R.F. Haglund, S.T. Pantelides, K.I. Bolotin, *Nano Lett.* **13**, 3626–3630 (2013)
 64. A. Castellanos-Gomez, R. Roldán, E. Cappelluti, M. Buscema, F. Guinea, H.S.J. van der Zant, G.A. Steele, *Nano Lett.* **13**, 5361–5366 (2013)
 65. S.N. Shirodkar, U.V. Waghmare, *Phys. Rev. Lett.* **112**, 157601 (2014)
 66. K.S. Novoselov, D. Jiang, F. Schedin, T.J. Booth, V.V. Khotkevich, S.V. Morozov, A.K. Geim, *Proc. Natl. Acad. Sci. USA* **102**, 10451–10453 (2005)
 67. D. Jena, A. Konar, *Phys. Rev. Lett.* **98**, 136805 (2007)
 68. M.S. Fuhrer, J. Hone, *Nat. Nanotechnol.* **8**, 146–147 (2013)
 69. S. Kim, A. Konar, W.-S. Hwang, J.H. Lee, J. Lee, J. Yang, C. Jung, H. Kim, J.-B. Yoo, J.-Y. Choi, Y.W. Jin, S.Y. Lee, D. Jena, W. Choi, K. Kim, *Nat. Commun.* **3**, 1011 (2012)
 70. K. Kaasbjerg, K.S. Thygesen, K.W. Jacobsen, *Phys. Rev. B Condens. Matter Mater. Phys.* **85**, 115317 (2012)
 71. M.R. Laskar, D.N. Nath, L. Ma, E.W. Lee, C.H. Lee, T. Kent, Z. Yang, R. Mishra, M.A. Roldan, J.-C. Idrobo, S.T. Pantelides, S.J. Pennycook, R.C. Myers, Y. Wu, S. Rajan, *Appl. Phys. Lett.* **104**, 092104 (2014)
 72. K. Dolui, I. Rungger, C. Das Pemmaraju, S. Sanvito, *Phys. Rev. B Condens. Matter Mater. Phys.* **88**, 075420 (2013)
 73. H. Fang, M. Tosun, G. Seol, T.C. Chang, K. Takei, J. Guo, A. Javey, *Nano Lett.* **13**, 1991–1995 (2013)
 74. B. Radisavljevic, A. Kis, *Nat. Mater.* **12**, 815–820 (2013) (**111**)
 75. D.Y. Qiu, F.H. da Jornada, S.G. Louie, Optical spectrum of MoS₂: many-body effects and diversity of exciton states. *Phys. Rev. Lett.* **111**, 216805 (2013)
 76. A. Ramasubramaniam, *Phys. Rev. B* **86**, 115409 (2012) 114
 77. X. Li, J.T. Mullen, Z. Jin, K.M. Borysenko, M. Buongiorno, Nardelli, K.W. Kim, *Phys. Rev. B* **87**, 115418 (2013)
 78. A. Marini, *Phys. Rev. Lett.* **101**, 106405 (2008)
 79. F. Ye, J. Lee, P. X.-L. Feng, Atomic layer MoS₂-graphene van der Waals heterostructure nanomechanical resonators. *Nanoscale* **9**, 18208–18215 (2017)
 80. M.Y. Li, Y. Shi, C.C. Cheng, L.S. Lu, Y.C. Lin, H.L. Tang, M.L. Tsai, C.W. Chu, K.H. Wei, J.H. He, W.H. Chang, K. Suenaga, L.J. Li, *Science* **349**, 524–528 (2015)
 81. C.H. Lee, G.H. Lee, A.M. van der Zande, W. Chen, Y. Li, M. Han, X. Cui, G. Arefe, C. Nuckolls, T.F. Heinz, J. Guo, J. Hone, P. Kim, *Nat. Nanotechnol.* **9**, 676–681 (2014)
 82. F. Pizzocchero, L. Gammelgaard, B.S. Jessen, J.M. Caridad, L. Wang, J. Hone, P. Bøggild, T.J. Booth, *Nat. Commun.* **7**, 11894 (2016)
 83. R. Yang, X. Zheng, Z. Wang, C.J. Miller, P.X.L. Feng, *J. Vac. Sci. Technol. B Nanotechnol. Microelectron. Mater. Process. Meas. Phenom.* **32**, 61203 (2014)
 84. J.A. Robinson, *ACS Nano* **10**, 42–45 (2016)
 85. L.Z. Hao, W. Gao, Y.J. Liu, Z.D. Han, Q.Z. Xue, W.Y. Guo, J. Zhu, Y.R. Li, High-performance n-MoS₂/i-SiO₂/p-Si heterojunction solar cells. *Nanoscale* **7**, 8304 (2015)
 86. G. Declerck, R. Van Overstraeten, G. Broux, *Solid State Electron.* **16**, 1451 (1973)
 87. T. Matsumoto, R. Hirose, F. Shibata, D. Ishibashi, S. Ogawara, H. Kobayashi, *Sol. Energy Mater. Sol. Cells* **134**, 298 (2015)
 88. D.J. Late, B. Liu, H.S.S. Ramakrishna Matte, C.N.R. Rao, V.P. Dravid, *Adv. Funct. Mater.* **22**, 1894 (2012)
 89. D.J. Late, B. Liu, H.S.S. Ramakrishna Matte, V.P. Dravid, C.N.R. Rao, *Adv. Funct. Mater.* **6**, 5635 (2012)
 90. G. Bugnon, G. Parascandolo, S. Hänni, M. Stuckelberger, M. Charrière, M. Despeisse, F. Meillaud, C. Ballif, *Sol. Energy Mater. Sol. Cells* **120**, 143 (2014)
 91. M.L. Tsai, S.H. Su, J.K. Chang, D.S. Tsai, C.H. Chen, C. Wu, L. Li, J. Chen, J.H. He, *ACS Nano* **8**, 8317 (2014)
 92. S.K. Pradhan, B. Xiao, A.K. Pradhan, *Sol. Energy Mater. Cells* **144**, 117 (2016)
 93. Z.Y. Yin, H. Li, L. Jiang, Y.M. Shi, Y.U. Sun, G. Lu, Q. Zhang, X.D. Chen, H. Zhang, *ACS Nano* **6**, 74 (2012)
 94. Q. Deng, Y. Li, Y. Shen, L. Chen, G. Weng, S. Wang, Numerical simulation on n-MoS₂/p-Si heterojunction solar cells. *Mod. Phys. Lett. B* **31**(7), 1750079 (2017)
 95. F. Xiong, H.T. Wang, X.G. Liu, J. Sun, M. Brongersma, E. Pop, Y. Cui, *Nano Lett.* **15**, 6777–6784 (2015)
 96. N. Ma, D. Jena, Carrier statistics and quantum capacitance effects on mobility extraction in two-dimensional crystal semiconductor field-effect transistors. *2D Mater.* **2**, 015003 (2015)
 97. Y. Gao, H.W. Liu, Y. Lin, G. Shao, *Thin Solid Films* **519**, 8490 (2011)